

Demographics of Tidal Disruption Events with L-Galaxies

I. Volumetric TDE rates and the abundance of Nuclear Star Clusters

M. Polkas^{1,2,*}, S. Bonoli^{1,3}, E. Bortolas^{4,5}, D. Izquierdo-Villalba^{4,5}, A. Sesana^{4,5,6}, L. Broggi^{4,5}, N. Hoyer^{1,7,8,9}, and D. Spinoso¹⁰

¹ Donostia International Physics Center, Paseo Manuel de Lardizabal 4, E-20118 Donostia-San Sebastián, Spain

² University of the Basque Country UPV/EHU, Department of Theoretical Physics, Bilbao, E-48080, Spain

³ IKERBASQUE, Basque Foundation for Science, E-48013, Bilbao, Spain

⁴ Dipartimento di Fisica ‘G. Occhialini’, Università degli Studi di Milano-Bicocca, Piazza della Scienza 3, I-20216 Milano, Italy

⁵ INFN, Sezione di Milano-Bicocca Piazza della Scienza 3, I-20126 Milano, Italy

⁶ INAF - Osservatorio Astronomico di Brera, via Brera 20, I-20121 Milano, Italy

⁷ Max-Planck-Institut für Astronomie, Königstuhl 17, D-69117 Heidelberg, Germany

⁸ Institute of Astronomy, Pontificia Universidad Católica de Chile, Avenida Vicuña Mackena 4690, Santiago, Chile

⁹ Universität Heidelberg, Seminarstrasse 2, D-69117 Heidelberg, Germany

¹⁰ Department of Astronomy, MongManWai Building, Tsinghua University, Beijing 100084, China

Received 2023; accepted 2023

ABSTRACT

Stars can be ripped apart by tidal forces in the vicinity of a massive black hole, causing luminous flares classified as tidal disruption events (TDEs). These events could be contributing to the mass growth of intermediate-mass black holes, while new samples from ongoing transient surveys can provide useful information on this unexplored growth channel. This work aims to study the demographics of TDEs by modeling the co-evolution of black holes and their galactic environments in a cosmological framework. We use the semi-analytic galaxy formation model L-Galaxies, which follows the evolution of galaxies as well as of massive black holes, including multiple scenarios for black hole seeds and growth, spin evolution, and binary black hole dynamics. Time-dependent TDE rates are associated with each black hole depending on the stellar environment, following the solutions to the 1-D Fokker Planck equation solved with PHASEFLOW. Our model produces TDE volumetric rates that are in agreement with the latest optical sample of 33 TDEs and previous X-ray samples. This agreement requires a high occupation fraction of nuclear star clusters with black holes since these star reservoirs host the majority of TDEs at all mass regimes. Unlike previous studies, we predict that TDE rates are an increasing function of black hole mass up to a peak of $\sim 10^{6.5} M_\odot$, beyond which rates drop following a shallow power-law distribution. In general, rates are predicted to be redshift-independent at $z < 1$. Yet, the TDE rates in active black holes of different levels of activity may evolve with redshift. We also discuss implications for the black hole spin distribution at the event horizon suppression and the cumulative growth due to TDEs. Our results highlight the need for time-dependent TDE rates, especially towards the low-mass regimes of the intermediate-mass black holes and dwarf galaxies.

Key words. black holes – tidal-disruption-events – nuclear-star-clusters – semi-analytic – galaxy evolution

1. Introduction

A tidal disruption event (TDE) occurs when a star wanders too close to a massive black hole (MBH) so that the MBH gravitational pull overcomes the star’s self-gravity. As a result, the star gets *spagettified*, as a part of it settles into a disk-like configuration producing a distinct, multi-wavelength electromagnetic flare. TDEs can outshine their host galaxies, with luminosities of $10^{42} - 10^{45} \text{ erg s}^{-1}$ which decline over weeks to years timescales. Most TDEs can be identified by the characteristic post-peak decrease of their accretion rate, which drops for most of the events as $\propto t^{-5/3}$, as predicted by the standard fallback theory (Rees 1988; Phinney 1989).

The first observations of TDE-like transients, initially in the X-ray (e.g. Bade et al. 1996; Komossa & Bade 1999; Esquej et al. 2008) and then in the optical/UV sky (Gezari et al. 2006, 2008; van Velzen et al. 2011), sparked the interest on their overall rate per galaxy (Magorrian & Tremaine 1999; Syer & Ulmer

1999; Wang & Merritt 2004). Such interest has grown even further at the present date, as the number of observed TDEs is growing faster than ever (we now have identified approximately 100 TDE candidates), mainly owing to the advent of wide-field transient optical surveys, such as Pan-STARRS1 (Chornock et al. 2014), the Palomar Transient Factory (PTF, e.g. Cenko et al. 2012; Arcavi et al. 2014), the ongoing Zwicky Transient Facility (ZTF, e.g. Lin et al. 2022; Hammerstein et al. 2023; Yao et al. 2023), and ASAS-SN (e.g. Krolik et al. 2016; Hinkle et al. 2021; Liu et al. 2023). In the X-rays, eROSITA has already provided a sample of candidates (Sazonov et al. 2021) adding to previously compiled inventories from Swift, XMM-Newton, and Chandra (Kawamuro et al. 2016; Auchettl et al. 2017; Goldtooth et al. 2023). Finally, individual dust-shrouded TDE candidates have been detected in mid-infrared (Maitla et al. 2018; Kool et al. 2020; Wang et al. 2022; Panagiotou et al. 2023), and a recent analysis of NEOWISE data has yielded the first sample at this wavelength (Masterson et al. 2024, reported as this work was submitted).

* markos.polkas@dipc.org

The collection of these growing samples has allowed us to assess the TDE rates. In particular, the works of van Velzen (2018), Lin et al. (2022) and Yao et al. (2023) used a relatively wide sample of observed TDEs to infer an overall volumetric rate of $\sim 10^{-7} - 10^{-6} \text{ Mpc}^{-3} \text{ yr}^{-1} \text{ dex}^{-1}$, corresponding to a number of TDEs per galaxy of the order of $10^{-5} - 10^{-4} \text{ yr}^{-1}$. Although these results necessarily depend on the shape of the TDE luminosity function, which remains uncertain, the obtained rates are in decent agreement with (although somewhat lower than) the TDE rates predicted by theoretical and numerical studies (Syer & Ulmer 1999; Magorrian & Tremaine 1999; Donley et al. 2002; Wang & Merritt 2004; Esquej et al. 2008; Merritt 2009; Brockamp et al. 2011; Stone & Metzger 2016; Pfister et al. 2021; Broggi et al. 2022). Nevertheless, both observational and theoretical estimates suffer from several limitations. On one side, the available sample of observed TDEs is still relatively small. On the other hand, for simplicity, theoretical models typically neglect important ingredients such as the time evolution of TDE rates under the evolution of the host galaxy. Most models are also affected by our poor knowledge of the MBH mass function at low masses ($\lesssim 10^7 M_\odot$) and the occupation fraction of nuclear star clusters (NSCs).

Still, currently available samples have allowed us to perform statistical studies on the host galaxies of observed TDEs (see French et al. 2020b for a review). In particular, ZTF observations have shed light on the fact that TDEs are over-represented in ultra-luminous Infrared Galaxies (ULIRGs, Tadhunter et al. 2017; Reynolds et al. 2022) as well as in the rarer post-starburst/green-valley galaxies (Hammerstein et al. 2021, 2023), and in particular in the quiescent Balmer-strong (E+A) ones (Arcavi et al. 2014; French et al. 2016; Law-Smith et al. 2017; Graur et al. 2018; Dodd et al. 2021). The stellar mass distribution of TDE-hosts is relatively flat compared to the stellar mass function and is concentrated at the dwarf-to-massive transition regime, $\sim 10^9 - 10^{11} M_\odot$ (Wevers et al. 2019). Interestingly, the occupation fraction of NSCs peaks in the same mass range (e.g. Sánchez-Janssen et al. 2019; Hoyer et al. 2021). That being said, MBHs and NSCs frequently have been related in many works (Antonini et al. 2015; Naiman et al. 2015; Trani et al. 2018; Askar et al. 2022; Atallah et al. 2023; Lee et al. 2023; Tremmel et al. 2023), yet the exact nature of their connection remains unknown. What seems to be evident from theoretical studies (Merritt 2009; Stone & Metzger 2016; Pfister et al. 2020), is that the presence of an NSC, the densest stellar system possible in the universe (Neumayer et al. 2020), may enhance the rate of TDEs on the central MBH. Therefore, the majority of TDEs are expected to be related to intermediate-mass black holes (typically defined as $10^{2.5} - 10^6 M_\odot$) at the center of NSCs. At this intermediate MBH-mass scale, the majority (>90%) of black holes are believed to be inactive (Greene et al. 2020), making samples inferred from AGN observations incomplete. Moreover, mass measurements through spectral information become troublesome at low masses (Kormendy & Ho 2013). In fact, beyond the local universe where accurate dynamical measurements of MBH mass can be made, TDE observations serve as the only *direct* detection method of the dormant MBH population, as opposed to the indirect method of detecting relic AGN activity.

Finally, TDEs offer a new viable channel of black hole growth (Hills 1975) that could in principle be dominant for MBHs that do not grow efficiently through gas accretion. After the first observations, the TDE growth channel was revisited (Magorrian & Tremaine 1999), with Milosavljević et al. (2006) proposing that low-mass MBHs ($< 2 \times 10^6 M_\odot$) may acquire the majority of their mass through TDEs. Furthermore, Alexan-

der & Bar-Or (2017) used this channel to set a lower limit on the masses of MBHs that can exist in the local universe since all MBH seeds should grow either through gas or TDEs. The initial growth through TDEs has been also studied within zoom-in cosmological simulations (Pfister et al. 2021; Lee et al. 2023) and, recently, N-body simulations achieved growing a black hole seed by a factor of > 20 within 1 Gyr (Rizzuto et al. 2023). Yet, the argument of effective TDE growth has been questioned for low-mass galaxies, since NSCs which contribute mainly to the TDE rates are not dense enough to fuel black hole growth by runaway tidal capture of NSC stars (Miller & Davies 2012; Stone et al. 2017). Nevertheless, a statistical study on the frequency of TDEs across a realistic population of stellar environments and the role of stellar accretion in the growth of MBHs has not been performed so far.

In this paper, we set the foundation to address many of the aforementioned theoretical uncertainties by combining, for the first time, a semi-analytic model of galaxy/black hole evolution in a wide range of stellar environments with time-dependent TDE rates provided by a fast 1D-Fokker Planck solver. The paper is structured as follows; In Sect. 2 we describe our method for coupling the physics of TDEs in a given local environment with a variety of stellar environments. In Sect. 3 we describe our most important findings and compare our TDE rate predictions with new constraints. In particular, we focus on the cosmological evolution of TDE rates and the contribution from active MBHs. In Sect. 4, we complement our analysis by addressing the impact of the parameter choice and discussing the implications for the occupation fraction of NSCs, the MBH spin model, and MBH growth. In Sect. 5, we discuss some caveats and subjects that we aim to investigate explicitly in the future. Finally, we summarize the key aspects of our work in Sect. 6. Throughout the paper, we adopt a Lambda Cold Dark Matter (Λ CDM) cosmology with parameters $\Omega_m = 0.315$, $\Omega_\Lambda = 0.685$, $\Omega_b = 0.0493$, $\sigma_8 = 0.826$ and $H_0 = 67.4 \text{ km s}^{-1} \text{ Mpc}^{-1}$ (Planck Collaboration et al. 2020).

2. Model Description

In this work, we combine the semi-analytical model of galaxy formation *L-Galaxies* with the 1D Fokker-Planck solver PHASEFLOW to estimate the time evolution of TDE rates and compare it with observations. In particular, we use a version of *L-Galaxies*, dubbed as *L-Galaxies* throughout this work, developed to study a wide variety of physical processes that drive the evolution of the MBH population and its co-evolution with galaxies. In this section, we first describe the *L-Galaxies* models and the additional physics included to model the TDE statistics. We then describe PHASEFLOW and how it is linked to *L-Galaxies* to assign TDE rates to MBHs.

2.1. The *L-Galaxies* semi-analytic models: Dark matter merger trees & baryonic physics

The *L-Galaxies* semi-analytic model is a well-tested model that tracks the cosmological evolution of the baryonic component of the Universe on top of dark matter merger trees (Croton et al. 2006; Guo et al. 2011; Henriques et al. 2015, 2020). It has been developed on, and is mainly being applied to, the dark matter merger trees of the *Millennium-I* (MS, Springel et al. 2005) and *Millennium-II* (MSII, Boylan-Kolchin et al. 2009) cosmological N-body simulations. In this work, we use the merger trees of the MSII which offer a higher mass resolution compared to the MS

simulation. Specifically, the MSII has a dark matter particle resolution of $6.89 \times 10^6 h^{-1} M_\odot$ in a box size of $100 h^{-1} \text{Mpc}$, enabling a good tracing of the cosmological evolution of halos where MBHs of $10^4 - 10^8 M_\odot$ are placed. Originally, the MSII was run by using the WMAP1 & 2dFGRS “concordance” ΛCDM framework (Spergel et al. 2003). However, the version of *L-Galaxies* used here applies the Angulo & White (2010) methodology to re-scale it to the cosmology of Planck 2018 data release (Planck Collaboration et al. 2020). This re-scaling modifies by a factor of 0.96 and 1.12 the MSII box size and particle mass, respectively.

Regarding the baryonic component, *L-Galaxies* follows the current paradigm of galaxy evolution which assumes that, as soon as a dark matter halo collapses, collapse within it (White & Frenk 1991). During this process, the infalling baryons are heated up and distributed inside the dark matter halo in the form of a diffuse, spherical, and quasi-static hot gas atmosphere. With time, this gas is allowed to cool down and migrate towards the center of the halo at a rate that depends on redshift and halo mass (White & Rees 1978; Sutherland & Dopita 1993). Due to angular momentum conservation, the cooled gas settles in a disk-like structure characterized by a radially exponential distribution. Once the disk becomes massive enough, star formation is triggered giving rise to a stellar component distributed in a disk with specific angular momentum inherited from the cold gas (Croton et al. 2006). Right after any star formation event, massive and short-lived stars explode polluting the interstellar medium and injecting energy in their environment, which can warm up and/or eject part of the cold gas of the disk. As a consequence of the ongoing stellar disk growth, some galaxies are prone to become unstable, with the subsequent disk instabilities leading to the formation of a stellar bulge component (Efsthathiou et al. 1982). Besides supernova explosions, *L-Galaxies* assumes that MBHs at the center of the galaxy can prevent the gas from cooling in massive galaxies by injecting kinetic energy into the surrounding medium via quiescent gas accretion directly from the hot gas component (dubbed as radio mode accretion Croton et al. 2006), thus hampering the supply of cold gas to a galaxy’s disk. On top of secular processes, *L-Galaxies* models the interactions between galaxies, occurring after a given time of the fusion of their parent DM halos. Such interactions include major and minor galaxy mergers and alter the structure of the remnant galaxy by triggering bursts of star formation and leading to the formation of a stellar bulge or pure elliptical structure. Finally, *L-Galaxies* also takes into account environmental processes such as ram pressure stripping or galaxy disruptions in its galaxy formation paradigm (Henriques et al. 2015).

To improve the time resolution offered by the outputs of the MSII simulation, *L-Galaxies* does an internal time interpolation between two consecutive snapshots, with the time resolution being $dt_{\text{step}} \sim 5 - 20 \text{ Myr}$, depending on redshift.

2.1.1. Massive Black Holes in L-Galaxies

The version of *L-Galaxies* used in this work (L-Galaxies) is based on the one presented in Henriques et al. (2015) with the modifications included in Izquierdo-Villalba et al. (2019, 2020, 2022) and Spinoso et al. (2023) to incorporate detailed massive black hole physics.

In brief, with respect to the model presented in Henriques et al. (2015), this new version adds a detailed model for the assembly (mass and spin) of nuclear MBHs, the dynamical evolution of MBH binaries, and the production of wandering MBHs (see Izquierdo-Villalba et al. 2020, 2022). Concerning the genesis of the first MBHs, L-Galaxies models the spatial vari-

ations of the intergalactic metallicity and the Lyman-Werner background¹ produced by star formation events to account for the formation of *heavy* (i.e. $M_{\text{seed}} \sim 10^5 M_\odot$) and *intermediate-mass* ($M_{\text{seed}} \sim 10^3 - 10^4 M_\odot$) MBH-seeds, respectively via the collapse of pristine massive gas clouds and runaway stellar mergers within dense high-redshift² NSCs. The formation of *light seeds* ($M_{\text{seed}} \sim 10^2 M_\odot$) after the explosion of the first metal-free stars (PopIII) is accounted for by grafting/inheriting the evolved counterparts of light-seed modeled self-consistently by the GametQSO/dust model (see e.g. Valiante et al. 2016). We note that concerning the black hole seeding model presented in Spinoso et al. (2023), we adopt a slightly higher amplitude of the “grafting probability”, setting the parameter $G_p = 0.25$ (see Spinoso et al. 2023, for the definition of this parameter). This choice is motivated by the normalization of the $z = 0$ black hole mass function in the current work.

Once the first MBH seeds are formed, galaxy mergers and disk instabilities funnel new gas to the galactic nuclei, making it available for the growth of nuclear MBHs. The gas reaching the center is progressively consumed by the MBH first in an Eddington limited phase, followed by a sub-Eddington one (Bonoli et al. 2009; Izquierdo-Villalba et al. 2020). Episodes of gas accretion, on top of triggering BH growth, also modify its spin (Izquierdo-Villalba et al. 2020). While L-Galaxies can track the evolution of wandering MBHs, we do not include that in this work for simplicity.

As an example of the capability of L-Galaxies to produce a realistic population of MBHs, in Fig. 1 we show the MBH mass function $\phi(M_\bullet)$, where M_\bullet is the black hole mass (throughout this work), and the MBH median spin distribution $\tilde{\chi}_\bullet(M_\bullet)$ at $z = 0$ and $z = 5.5$ for the version of L-Galaxies adopted in the current work. We compare our results with available data. Regarding the black hole mass function, as noted by Shankar et al. (2019), all observationally-derived values seem to converge at the high mass-end ($M_\bullet > 10^{7.5} M_\odot$ Merloni & Heinz 2008; Cao 2010; Gallo & Sesana 2019; Shankar et al. 2009, 2013; Mutlu-Pakdil et al. 2016; Vika et al. 2009; Aversa et al. 2015). However, constraints at the intermediate-mass range $M_\bullet \sim 10^5 - 10^6 M_\odot$ are much less stringent. L-Galaxies agrees with the most optimistic estimates from Shankar et al. (2009) and over-estimates with respect to all other available constraints. Regarding the spin distribution, the model agrees with the constraints from Reynolds (2021) at high masses, yet it predicts high-to-maximal spin for MBHs at the intermediate mass range, where there are no observational constraints. TDEs can potentially offer as a new probe for both the MBH mass and spin distribution in this range (see discussion in Sect. 4.3).

2.1.2. The Stellar Environment of Massive Black Holes

As mentioned above, the novelty of this work is the inclusion of TDEs within a full galaxy evolution context. To encompass this ambitious task it is necessary to model the stellar environment in which MBHs are embedded, on top of their formation and evolution. In this section, we describe how disks, bulges, and NSCs are included in L-Galaxies. Together with black hole masses,

¹ The Lyman-Werner (LW) band is a specific energy-interval (i.e. $h\nu = [11.2 - 13.6] \text{eV}$) in the UV spectrum. LW photons are responsible for the photo-dissociation of molecular hydrogen (e.g. Haiman et al. 1997).

² not to be confused with the ones introduced later in this work, for which we follow a different treatment

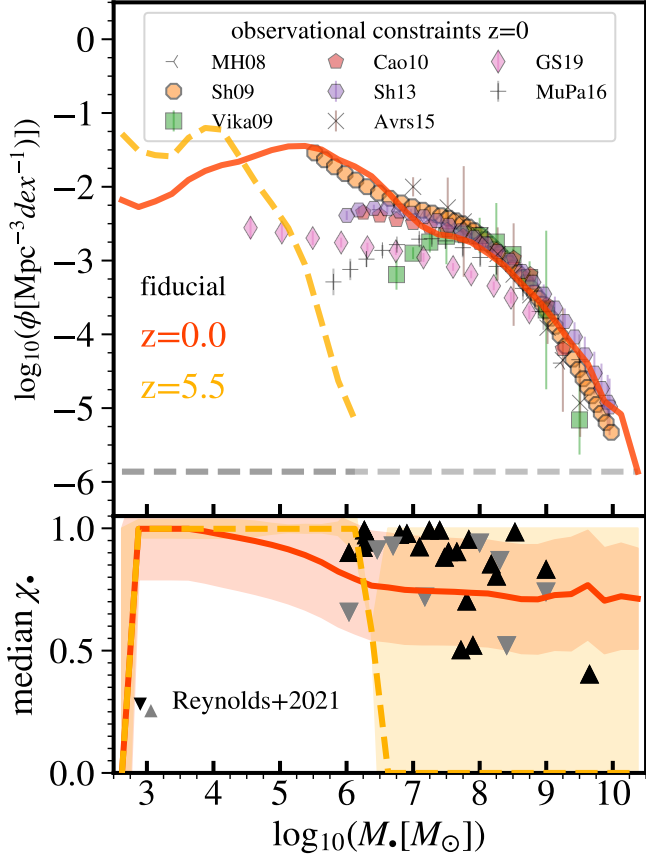


Fig. 1. MBH mass function (top) and median spin for X-ray bright MBHs (bottom) as a function of the MBH mass M_* predicted by the L-Galaxies model used in this work; data are shown for $z=0$ (red solid line) and $z=5.5$ (yellow dashed line), with shaded areas in the bottom panel referring to the 1σ dispersion at a given mass range. In the top panel, the grey dashed line corresponds to the MBH mass function value equal to 1 dex^{-1} per MSII simulation volume; the results are compared with observational data at $z=0$: MH08, Vika09, Sh09, Cao10, Sh13, Avrs15, GS19, MuPa16 refer to the model-dependent constraints on the MBH mass function derived respectively by Mergoni & Heinz (2008), Cao (2010), Gallo & Sesana (2019), Shankar et al. (2009), Shankar et al. (2013), Mutlu-Pakdil et al. (2016), Vika et al. (2009), Aversa et al. (2015). For spin constraints, we display the upper and lower limits from X-ray reflection spectroscopy (Reynolds 2021). For a closer comparison to observational results, the average spin values shown here are for MBHs with a predicted hard X-ray luminosity of $\log L_{\text{HX}} > 40 \text{ erg s}^{-1}$.

the properties of the nuclear stellar environment will be the input for predicting time-evolving TDE rates with *PhaseFlow*.

Bulge and Disk profiles in L-Galaxies

Bulges in L-Galaxies grow after galaxy interactions (major and minor mergers) and disk instabilities occurring in massive stellar disks. The specific properties of these events fully determine the final mass and extension (i.e. effective size) of the bulge. We stress that the scale length for disks $R_{\text{eff,d}}$ and the effective size of bulges $R_{\text{eff,b}}$ (equivalent to the scale radius of a Sérsic profile) are computed self-consistently inside L-Galaxies by tracing the spin evolution of the galaxy components and applying energy conservation during mergers and disk instabilities. The profile of each bulge is assumed to follow a Sérsic model, whose steepness (i.e. Sérsic index) is associated with each bulge by us-

ing the observational results of Gadotti (2009), approximately a Gaussian distribution peaking at Sérsic index $n_s = 3 - 4$, as implemented in Izquierdo-Villalba et al. (2019). As already mentioned, galactic disks arise as a consequence of gas cooling and star formation events occurring at the center or dark matter halos. Together with galaxy encounters, these events determine the extent of the disk radial profile. Taking this into account, in this work we assume that pure disks with no bulge are characterized by the Sérsic index $n_s = 1$, regardless of redshift, and a scale radius of $R_{\text{gal}} = 1.68 R_{\text{eff,d}}$. For the rest of this work, we refer to the sum of the disk and bulge mass as galaxy stellar mass M_* (the halo and intracluster stellar mass are neglected during our analysis), while M_{gal} is reserved for the integrated mass of a Sérsic profile (either a bulge or a disk) with radius R_{gal} . As we will see later, TDE events due to encounters between the nuclear MBHs and stars belonging to the bulge or disk component will be calculated assuming that these density profiles extend to the center.

Nuclear Star Clusters in L-Galaxies

NSCs observed at the centers of a great fraction of dwarf and massive galaxies in the local Universe are the densest stellar structures known (see Neumayer et al. 2020, for a review). This inevitably suggests that they might be an ideal nursery for TDEs. In the following paragraphs, we describe a simple *phenomenological model* that we are introducing in L-Galaxies to incorporate NSCs in galaxies (“nucleation”). An extensive and self-consistent modeling of the birth and evolution of NSCs will be presented in a future paper (Hoyer et al. in prep).

NSC Mass: The mass of an NSC, M_{NSC} , is a fundamental property to be determined. To this end, we connect the NSC mass with the total galaxy stellar mass M_* of the host system via the following relation derived from observations of clusters in the local universe:

$$\log_{10}(M_{\text{NSC}}/M_{\odot}) = A + B \log_{10}(M_*/10^{9.4}M_{\odot}) \quad (1)$$

with

$$A = 6.684 \quad \& \quad B = \begin{cases} 0.94, & \text{if } M_* > 10^{9.4}M_{\odot} \\ 0.55, & \text{if } M_* \leq 10^{9.4}M_{\odot} \end{cases}.$$

The high mass end of this relation is obtained from the work of Pechetti et al. (2020), while the lower mass end is adapted to the results from Hoyer et al. (2023). We also introduce a 0.5 dex uniform scatter to these median values, comparable to the scatter of 0.23 dex measured by Pechetti et al. (2020) to their relation as well as to the uncertainty on the assumed mass-to-light ratio of about 0.3 dex (Roediger & Courteau 2015).

To avoid the formation of too many small clusters, we impose a minimum mass limit $M_{*,\text{NSC}}^{\text{min}} = 5 \times M_{\text{jeans}}(z)$ where $M_{\text{jeans}}(z)$ is the redshift-dependent Jeans mass for cold gas in the absence of a heat bath. This factor of 5 is arbitrary and kept fixed through this work. To avoid unphysically massive NSCs, we also impose a maximum mass limit of $M_{*,\text{NSC}}^{\text{max}}$ equal to 95% that of the galaxy component (bulge, or disk in the absence of bulge) M_{gal} .

Nucleation: In this work, we make the simple assumption that only galaxies with an MBH can host an NSC, although we are fully aware that the frequency of co-existence of MBHs and NSCs is observationally not yet fully established, with only a

handful of NSCs with MBHs being detected in the same galaxy (Seth et al. 2008; Graham & Spitler 2009; Neumayer & Walcher 2012; Georgiev et al. 2016; Nguyen et al. 2018; Kimbrell et al. 2021; Nguyen et al. 2022; Ashok et al. 2023; Thater et al. 2023).³ In our toy model, galaxies hosting an MBH can also host an NSC depending on a simple step-function probability:

$$P(M_*, z) = P_0, \text{ for } M_{*,\text{NSC}}^{\min} < M_* < M_{*,\text{NSC cut-off}} \quad (2)$$

where $M_{*,\text{NSC cut-off}}$ is a cut-off mass and P_0 is a free parameter. For our *fiducial* model, we assume $P_0 = 1$. For the case of $M_{*,\text{NSC cut-off}}$ our *fiducial* model uses the value $10^{9.75} M_\odot$ motivated by the theoretical work of Antonini et al. (2015) and the observations of the Local Volume and close galaxy clusters (see e.g. Hoyer et al. 2021).

After formation, we assume that NSCs do not change in mass if the galaxy is evolving secularly (see discussion in Sect. 2.3.2) or experiences only minor mergers (in this case, the NSC of the central galaxy acquires the NSC of the merged satellite, following the dynamics of the companion MBH). Indeed, NSCs are extremely compact stellar systems and are expected to be difficult to be destroyed from external tidal fields during mergers (see the works of Bassino et al. 1994; Pfeffer et al. 2014; Mayes et al. 2021, for the detection of stripped nuclei).

Following these assumptions, the model predictions for the NSC occupation fraction at $z = 0$ for all galaxies hosting an MBH and for the full population are shown in Fig. 2. Regarding galaxies hosting an MBH, we see that below the cut-off galaxy stellar mass $M_{*,\text{NSC cut-off}}$, all galaxies also host an NSC, by construction. Above the cut-off mass, NSCs are present only in galaxies that were smaller at the time of NSC formation and then evolved secularly in stellar mass (see discussion in Sect. 2.3.2). When looking at the occupation fraction of the full galaxy population, instead, we see that dwarf galaxies are less likely to host an NSC because of the lower MBH occupation fraction. This is what is driving the total NSC occupation fraction to increase with galaxy mass until approximately the cut-off mass, naturally following the logistic function that is fitted to the observations of Hoyer et al. (2021) up to $M_* = 10^{9.5} M_\odot$.

2.2. From galaxy properties to time-dependent TDE rates with PhaseFlow

Black hole masses, and the properties of the nuclear stellar component of galaxies, modeled in L-Galaxies as described above, provide the starting point for the calculation of time-dependent TDE rates.

The main, ubiquitous generation mechanism for TDEs is thought to be two-body relaxation (Chandrasekhar 1942; Frank & Rees 1976; Binney & Tremaine 2008). In simple terms, stars in the vicinity of an MBH deflect each other's orbits so that a star may eventually reach a very small pericentre, closer than the tidal disruption radius, defined as

$$r_t \approx \left(\frac{M_\bullet}{m_\star} \right)^{1/3} r_\star \quad (3)$$

and be disrupted by the MBH of mass M_\bullet ; here m_\star is the stellar mass and r_\star its radius. The occurrence of these events can be described in terms of the *loss cone theory* (see e.g. Merritt 2013; Stone et al. 2020), adopting a Fokker-Planck approach. In

³ Notice the existence of a few nearby galaxies hosting an NSC but lacking an SMBH: M 33 (Gebhardt et al. 2001; Merritt et al. 2001), M 110 (Valluri et al. 2005), or NGC 7793 (Neumayer & Walcher 2012).

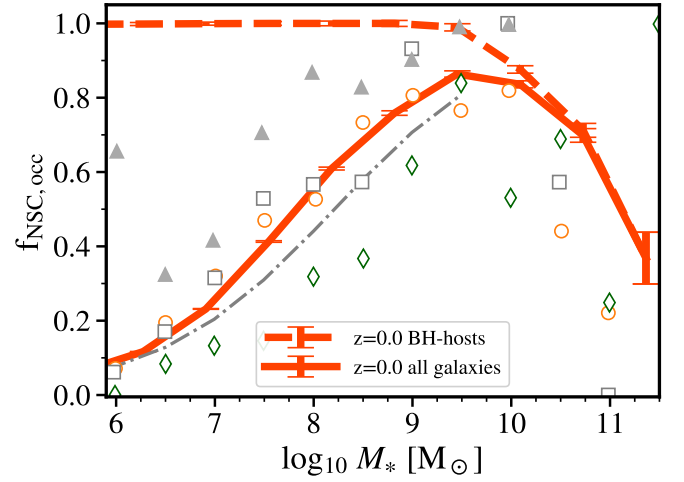


Fig. 2. The NSC occupation fraction for our *fiducial* model as a function of galaxy stellar mass, for all galaxies (solid line) and all galaxies hosting an MBH (dashed line). All $M_* < 10^9 M_\odot$ galaxies hosting an MBH have also a 100% probability of hosting an NSC at creation. The data represents the NSC occupation fraction for the Virgo (orange circles), Fornax (white squares), Coma (grey triangles) clusters, and the Local Volume (green rhombuses) as presented in Hoyer et al. (2021). Our model fits the logistic function for NSC occupation at $M_* < 10^{9.5} M_\odot$ of the same work (thin grey line). We stress that this agreement occurs naturally from the occupation of MBHs per galaxy (see discussion in Sec.4.2).

particular, in the present work, we make use of the PHASEFLOW code (Vasiliev 2017), which is part of the AGAMA toolkit (Vasiliev 2019). PHASEFLOW evolves in time an isotropic and spherically symmetric stellar distribution⁴ $f(E)$ by solving the Poisson and orbit-averaged Fokker–Planck 1-D equations for the stellar distribution function, its gravitational potential, and its density. A sink term mimics stellar accretion onto the MBH, which grows in mass as a result. To account for the production of TDEs at this sink term, at each timestep the rate of TDEs associated with $f(E)$ is computed from a different (anisotropic) profile $f(E, J)$ that assumes the relaxed, logarithmic profile in angular momentum (Cohn & Kulsrud 1978). PHASEFLOW has been extensively used in the framework of inferring TDE rates, including addressing the impact of the stellar mass function on TDE rates (Bortolas 2022) as well as predicting realistically partial disruption event rates (Bortolas et al. 2023).

2.2.1. PhaseFlow set-up

In our implementation, we assume that the stellar system surrounding the MBH is composed by a bi-chromatic population of stars made up of main-sequence stars of $0.38 M_\odot$ (encompassing $\approx 97\%$ of the total stellar mass) and $16 M_\odot$ stellar black holes⁵

⁴ The energy dependence only means that at any instant the distribution function only depends on the energy of an orbit E . Particles with the same energy are assumed to follow the so-called thermal distribution of angular momentum J , which is uniform in squared angular momentum; this distribution is used to compute the evolution of the profile (and in particular the diffusion coefficients).

⁵ The choice for these values for the mass of main sequence stars and stellar black holes comes from the fact that those are close to the average masses for those objects assuming an evolved Kroupa (2001) stellar mass function; in addition, the second moment of the mass function, which sets the relaxation rate of the system and thus the TDE rates, attains a value which is very close to the actual one if we were to assume

(encompassing the remaining $\approx 3\%$). Stars are considered to be destroyed if their separation to the MBH gets below r_t (Eq. 3), where we used $r_\star = 0.44R_\odot$, which is the expected radius of a $0.38 M_\odot$ star (see e.g. Bortolas 2022, Eq. 3, for more details). Once accretion occurs, 30% of the stellar mass⁶ is added to the MBH, while the remainder is assumed to be lost in radiation and the interstellar medium. Stellar black holes are instead captured by the MBH if they get closer than $8GM_\bullet/c^2$ from the MBH, where c is the speed of light in vacuum and G the gravitational constant. During the evolution of the system, the stellar populations undergo the traditional dynamical phenomena expected in the vicinity to an MBH, i.e. they develop a Bahcall & Wolf (1976) cusp, stellar black holes segregate in the center dominating relaxation in the closest vicinity to the MBH and finally, once the system has reached a dynamical equilibrium, it typically expands and lowers its TDE rates as a result of dynamical heating. All these phenomena are captured by PHASEFLOW.

Given the fast performance of the code, we have generated multi-dimensional tables spanning a range of initial central MBH masses and a range of host-environment properties (mass, scale radius, compactness for disks, bulges, and NSCs), encompassing all values predicted by L-Galaxies, as described in what follows. In particular, all runs in the multi-dimensional grid were initially evolved for a Hubble time using 300 bins in the phase-volume, the variable used in the code to parameterize the distribution function⁷.

2.2.2. The PhaseFlow-generated grid of TDE rates

We model rates depending on their reservoir origin, which could be either a bulge/disk or an NSC. Rates are saved in a large multi-dimensional grid, which includes the parameter space of the MBH, the stellar environment properties, and the time dimension. Rates are *not static* but instead vary as time goes by (not necessarily a steady state is reached). This adds substantial realism to our computation as many systems dominating the overall TDE rate are often characterized by a very large initial rate which drops by orders of magnitude with time. Assuming the static rate (which would coincide with the $t = 0$ rate) thus results in a non-negligible overestimation of TDE rates, especially for the case of NSCs.

The parameter space mapped is the following:

MBH mass: The first input parameter is the central MBH mass. The grid covers the range:

$$\log_{10}(M_\bullet/M_\odot) \in [2.5, 8.0] \quad (4)$$

in 34 equally spaced logarithmic steps. Here, the upper limit lies at the high-mass end of the event-horizon suppression defined by the range of values of the Hills mass. This is the MBH mass for which the tidal radius is within the horizon

a complete and evolved stellar mass function (see e.g. Kochanek 2016; Stone & Metzger 2016; Pfister et al. 2022; Bortolas 2022).

⁶ At a full disruption, the MBH captures 50% of the stellar mass. We selected a subsequent mass loss due to radiation and winds removing 40% of the bound material based on results from observations (Mockler & Ramirez-Ruiz 2021) and simulations (Bu et al. 2023). Simulations including radiative transfer from Steinberg & Stone (2022) yield a lower percentage of 15%.

⁷ The phase-volume $h(E)$ is the volume in phase space spanned by all the orbits with energy E ; unlike the orbital energy it is invariant under adiabatic changes of the potential, like in the case of a central MBH accreting via TDEs, and this makes $h(E)$ a very good choice for this problem.

radius ($r_t < r_g$, Hills 1975). The Hills mass depends on the black hole spin and the infalling star properties and its orbit (Kesden 2012; Mummery 2024), but it is in the range $M_\bullet = 10^7 - 10^8 M_\odot$ for an $0.38 M_\odot$ star (see also Sect. 2.3.4).

Galaxy stellar component: To predict TDE rates, PHASEFLOW needs the galaxy stellar mass M_{gal} , the scale radius R_{gal} and Sérsic index n_s . We map stellar mass values in a broad range around the MBH mass M_\bullet values, following this scaling:

$$\log_{10}(M_{\text{gal}}/M_\bullet) \in [1, 4] \quad (5)$$

in 16 equally spaced logarithmic bins. The scale radius can instead vary in the range:

$$\log_{10}(R_{\text{gal}}/R_{\text{scl}}) \in [-2, 1] \quad (6)$$

with 13 equally spaced logarithmic bins, where R_{scl} depends on the stellar mass as (Shen et al. 2003):

$$\log_{10}(R_{\text{scl}}/\text{kpc}) = 0.14 \log_{10}(M_{\text{gal}}/M_\odot) - 1.21. \quad (7)$$

Finally, for the Sérsic index we assume all integer values between one and seven, which is the range we probe in L-Galaxies, as described in Sect. 2.1.2. This gives a grand total of $34 \times 16 \times 13 \times 7 = 49\,504$ combinations of parameters for the galaxy stellar component. For galaxies with both a disk and bulge component, the contribution of the disk to TDE rates is ignored, as it is generally significantly lower. Note, however, that small galaxies in L-Galaxies are often pure disks, and their contribution to the total volumetric rate is non-negligible.

NSCs: To estimate the TDE rates in an NSC environment with PHASEFLOW, the NSC mass M_{NSC} , effective radius $R_{\text{NSC,eff}}$ and density profile are needed. Given the mass range for the galaxy component considered in the above grid (Eq. 5), the NSC mass range follows by applying to this the scaling relation presented in Eq. 1 (from combining the works of Pechetti et al. 2020 and Hoyer et al. 2023). From Pechetti et al. (2020) we also use the definition of the NSC effective radius, which correlates with the galaxy stellar mass M_\star as:

$$\log_{10}(R_{\text{NSC,eff}}/\text{pc}) = 0.53 + 0.29 \log_{10}(M_\star/10^9 M_\odot). \quad (8)$$

We stress that this relation is especially holding towards the high-mass end but flattens out at low masses (Neumayer et al. 2020). To explore how the results presented in this work depend on the choice of fixed compactness of the NSC, we construct a second grid using $R_{\text{eff,NSC}}$ equal to 1/3 of the radius predicted by the scaling relation. We dub these additional runs as *compactNSC*. The *fiducial* model follows Eq. 8 and will be compared with the *compactNSC* one in Sect. 4.4. The initial NSC density profile is assumed to follow the functional forms of Saha (1992) and Zhao (1996):

$$\rho_{\text{NSC}}(r) = \rho_0 \left(\frac{r}{a}\right)^{-\gamma} \left[1 + \left(\frac{r}{a}\right)^\alpha\right]^{\frac{\gamma-\beta}{\alpha}} \exp\left[\left(-\frac{r}{r_{\text{cut}}}\right)^\xi\right]. \quad (9)$$

where ρ_0 is a normalization constant that ensures the total mass of the cluster is M_{NSC} , $a = R_{\text{NSC,eff}}/4.6$ is its scale radius, while $\alpha = 4$, $\beta = 2$, and $\gamma = 0.5$ are density slopes in different regions of the NSC. Finally, $r_{\text{cut}} = 12a$ is a cutoff radius and $\xi = 2$ represents the cutoff strength. The selected values have been chosen based on the results by Antonini et al. (2012), who explored the formation of NSCs through the infall of star clusters (see e.g.

Capuzzo-Dolcetta 1993; Hartmann et al. 2011; Arca-Sedda & Capuzzo-Dolcetta 2014; Sánchez-Janssen et al. 2019; Fahrion et al. 2022; Carlsten et al. 2022; Leaman & van de Ven 2022; Hoyer et al. 2023, on the connection between NSCs and globular clusters). This profile should thus be a valid resemblance to the profile of a recently-formed NSC.

Taking into account the scaling relations described above, it is clear that all NSC properties ultimately depend only on the galaxy stellar mass M_* . Thus, the grid for the TDEs due to NSCs spans only the values of M_\bullet and M_* , in the same ranges as mentioned for the galaxy stellar component above: total $34 \times 16 = 544$ pairs of parameters.

Once the runs with PHASEFLOW are completed and the grid in the parameter space has been fully mapped, we store the resulting event rates, Γ , which are a function of the aforementioned parameters and time t . For the bulge/disk contribution, the rates are encapsulated in the function $\Gamma_{\text{gal}}(M_{\text{gal}}, R_{\text{gal}}, n_s; M_\bullet, t)$, while for the NSCs, the rates are given by the function $\Gamma_{\text{NSC}}(M_{\text{NSC}}; M_\bullet, t)$. We note that we store only the time values in the range:

$$\log_{10}(t/\text{yr}) \in [7.0, 10.146] \quad (10)$$

with 50 evenly spaced logarithmic bins. We do not consider TDE rates at times below 10^7 yr given the time resolution of L-Galaxies which spans between $dt_{\text{step}} \sim 5 - 20$ Myr, depending on redshift.

In the following section, we outline how we merge L-Galaxies with the Γ_{gal} and Γ_{NSC} rates constructed from the multi-dimensional grid described above. To guide the reader, Fig. 3 shows several examples of the time-evolving TDE rates in a variety of black hole masses for a fixed set of parameters. In the figure, for each black hole mass, we assume that the corresponding galaxy mass is given from the relation $\log_{10}(M_\bullet/10^{7.43}M_\odot) = 0.62 \log_{10}(M_{\text{gal}}/10^{10.5}M_\odot)$, which is the best-fit relation we get in L-Galaxies at $z=0$ for MBHs up to $\sim 10^8 M_\odot$. The scale radius assigned to the Sérsic profile is here assumed to be an average value of $R_{\text{gal}} = R_{\text{scl}}$. The disk corresponds to $n_s = 1$ and the bulge to $n_s = 4$. The matching NSC profiles are created by using the scaling relations presented in Eq. 1 and Eq. 8.

As shown from Fig. 3, the main general feature of our model is that the typical, average rates increase with increasing MBH mass, as the stellar reservoirs assigned are increasingly more massive for more massive MBHs. However, there is a strong differentiation between the galaxy component and the NSC component; while bulges and disks profiles often obtain a constant event rate given the large relaxation timescale of these systems, NSCs matching to $M_\bullet < 10^6 M_\odot$ show decay in their initial TDE rate due to their fast relaxation dynamics. Typically, the decay happens earlier for smaller MBHs and smaller reservoirs. Notably, NSC with M_\bullet from $10^4 M_\odot$ to $10^6 M_\odot$ start with similar TDE rates at 10^7 yrs, but maintain it shorter times compared to the Hubble time, as the systems quickly reach their equilibrium in the form of a Bahcall & Wolf (1976) cusp and subsequently expand due to the dynamical heating resulting from efficient relaxation. In that aspect, the cut at 10^7 yr ignores strong TDE rates coming from small, fast-relaxing systems: for MBHs with $M_\bullet < 10^4 M_\odot$, the value estimated by steady-state is achieved only during an initial period of fast relaxation below our time resolution, and therefore the initial TDE production of these systems may be underestimated.

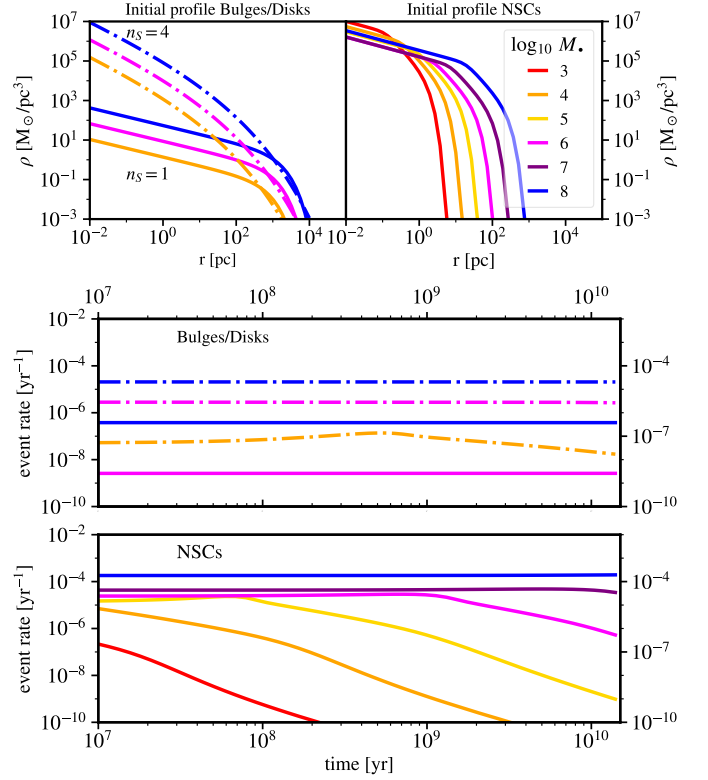


Fig. 3. *Top panels:* Stellar density profiles for a range of MBH masses as indicated in the inset legend (with the same color-coding applying to all panels of the figures). Disks are assigned $n_s = 1$ Sérsic profiles (solid lines, left) while bulges $n_s = 4$ profiles (dotted lines, left). NSCs are instead assigned spheroid profiles from Eq. 9 (right). The galaxy and NSC host properties scale with M_\bullet as described in the text and are created to be representative of the average environment encountered in L-Galaxies. *Middle & bottom panels:* Tidal disruption event rate evolution with PHASEFLOW when initiating for different MBH mass with the associated profiles from the top panels, displayed separately for bulges/disks (galaxy component, middle panel) and NSCs (bottom).

2.3. TDE rates in L-Galaxies

The final step consists of joining in a self-consistent way the TDE rates calculated by PHASEFLOW and the properties and stellar environments of MBH predicted by L-Galaxies. We schematically show this in Fig. 4, and we describe the details below.

2.3.1. Event rates and mass accretion

As soon as an MBH forms inside a galaxy in L-Galaxies, we set a TDE rate depending on the existence of a stellar bulge/disk and/or an NSC. Effectively, we look up the multi-dimensional grid generated with PHASEFLOW for the rate Γ_i , with $i = \text{gal}$ for the galaxy component and $i = \text{NSC}$ for the NSC. From this, we derive the time-evolving rates for each MBH and stellar environment. For galaxy and NSC properties we look up for the closest values in the grid, while we interpolate in the MBH and time dimension.⁸

When TDEs start being produced within a galaxy, either from the relaxation of the bulge/disk or the NSC, we start a

⁸ In only a few instances values predicted by L-Galaxies are outside the parameter space covered by the grid. In these rare cases, we use the closest valid value.

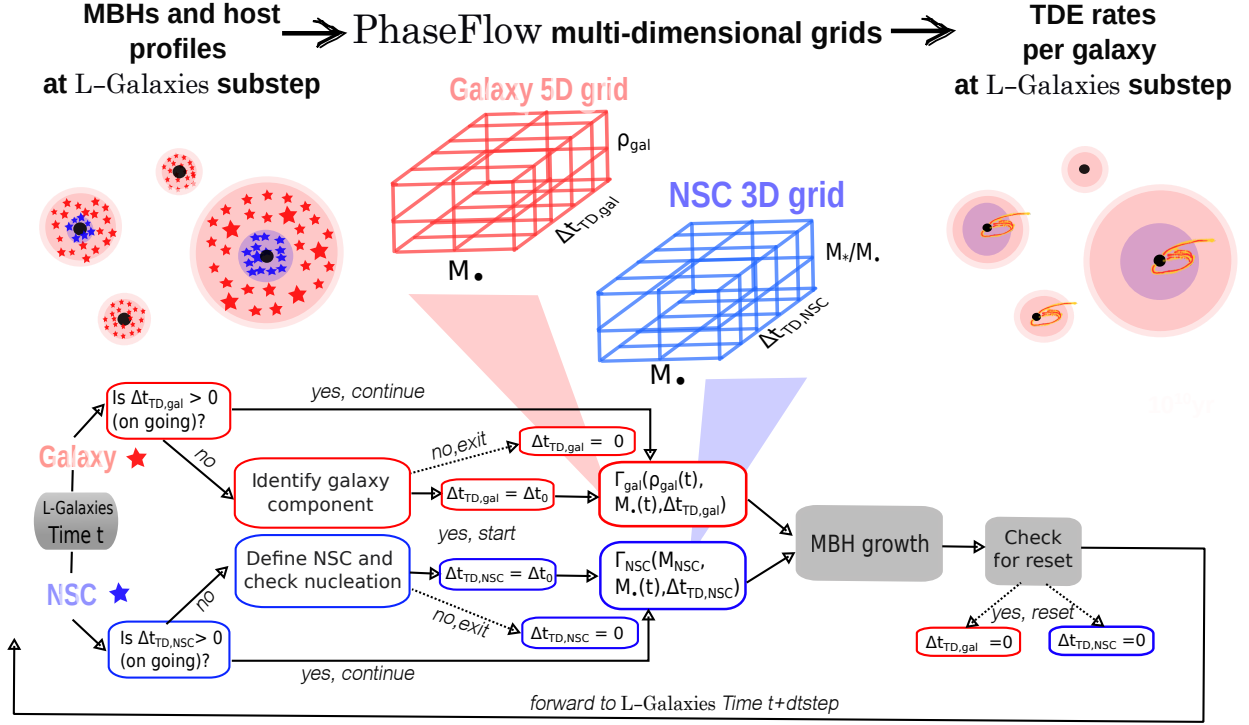


Fig. 4. Flowchart of the current scheme for estimating TDEs within a single time-step of L-Galaxies. The decision-making tree is colored red and blue for the galaxy (bulge or disk in the absence of bulge) and NSC components, respectively. With the density profile ρ_{gal} we refer to all galaxy component parameters $\{M_{\text{gal}}, R_{\text{gal}}, n_s\}$ that are used to initialize the Sérsic profile. TDE rates from the galaxy as a whole and its NSC are effectively treated independently (each process has its clock Δt_{TD}) and can be active at the same time, while they sum together to produce the instantaneous rate of each MBH.

clock, $\Delta t_{\text{TD},i}$ (with $i = \text{gal}$ for the galaxy component and $i = \text{NSC}$ for the NSC). In the successive steps of the L-Galaxies run, the PHASEFlow grid is checked at the corresponding subsequent times. As described in the next section, we reset this clock to zero only when the MBH and/or the galaxy have substantially changed, which can happen, for example, after mergers.

Next, we define the fraction of the stellar mass accreted by the MBH after it has been tidally disrupted:

$$f_{*,\text{TDE}} = \begin{cases} 0.3, & \text{if } M_{\bullet} \leq 10^8 M_{\odot} \\ 1, & \text{otherwise} \end{cases}.$$

We anticipate that the growth due to the accretion/capture of stars above the Hills mass⁹ is negligible, therefore the precise number of direct captures as a function of MBH mass will not change significantly our results. Also, this selection does not affect the results regarding TDE rates.

Provided the TDE rate and the accretion fraction per event, the mass accreted by the central MBH in each time-step of L-Galaxies is given by:

$$dM_{\bullet,\text{acc}} = dt_{\text{step}} \sum_i^{\text{gal,NSC}} \Gamma_i f_{*,\text{TDE}} m_* \quad (11)$$

⁹ as mentioned earlier, $M_{\bullet} = 10^8 M_{\odot}$ is the approximate mass limit for event-horizon suppression; beyond this MBH mass stars are not disrupted, therefore $f_{*,\text{TDE}} = 1$ instead of 0.3.

and the mass subtracted from each stellar component¹⁰ ($i = \text{gal}$ or $i = \text{NSC}$) is:

$$dM_{i,\text{loss}} = dt_{\text{step}} [\Gamma_i (+\Gamma_{\text{NSC}} \text{ if } i = \text{gal})] m_*. \quad (12)$$

Notice that, if both a bulge/disk and an NSC are present, we sum the two TDE rate contributions. The results of the mass growth of MBHs through this mechanism are discussed briefly in Sect. 4.1.

2.3.2. Conditions for changing/resetting TDE rates

Once TDEs start taking place, PHASEFlow is able to capture the time evolution of the stellar density profile as a result of relaxation and MBH growth due to star accretion. However, dramatic events, such as mergers, disk instabilities, and starbursts, can lead to major changes in the stellar environment surrounding the MBH. In these cases, we *reset* the clock for TDE rates ($\Delta t_{\text{TD},i}$), and the new, unrelaxed stellar system starts again evolving towards a new relaxed state until the next violent dynamical event.

The conditions under which we consider relevant to check the state of the TDE process taking place around an MBH (i.e., Γ_i and $\Delta t_{\text{TD},i}$) are the following ones:

Changes in MBH mass: If the mass accreted by the MBH via gas accretion is three times larger than the mass grown cumulatively by TDEs, then the $\Delta t_{\text{TD,NSC}}$ clock is reset again

¹⁰ Note that we consider an NSC as a decomposed part of the central bulge/disk, that we subtract separately from.

and the NSC mass and properties are adapted to the galaxy mass when this happens.¹¹

Changes in the galaxy component: The clock $\Delta t_{\text{TD,gal}}$ is reset if, from one L-Galaxies time-step to the next one, the bulge or disk stellar mass increases by more than 20%, which is a typical change in galaxy stellar mass in post-starburst galaxies (Kaviraj et al. 2007; van Velzen 2018; Wild et al. 2016, 2020). Note that events that do not modify the total stellar mass, but only the distribution into bulge and disk component, can lead to a reset of the rates (e.g., the transfer of mass from the disk to the bulge during disk instabilities). This process will not reset rates originating from NSCs since these can continue relaxing at their own pace unaffected by the changes in the galactic-scale environment.

Changes in NSC: As described in Sect. 2.1.2, an NSC can undergo significant mass changes following the host galaxy changes. Following the same approach described above, we select $\delta M_{\text{NSC}} / M_{\text{NSC}} > 20\%$ within one L-Galaxies time-step, as the condition of resetting the clock $\Delta t_{\text{TD,NSC}}$. This threshold is selected to be equal to that of the galaxy component in order to minimize the free parameters of the model. While there are no clear constraints on the limits of the mass ratio between an NSC and the MBH at its center, namely $\mathcal{D} = M_{\text{NSC}}/M_{\bullet}$, we decided to put a lower limit on this ratio so that an NSC gets to be (re)generated only if $\mathcal{D} > \mathcal{D}_{\text{nuc}}$. On one hand, the MBH formation in NSCs may limit \mathcal{D}_{nuc} to small values (e.g. runaway stellar collisions can reach ratios down to $\mathcal{D}_{\text{nuc}} \sim 1$ Kritos et al. 2023). On the other hand, the NSC destruction from binary MBHs (Antonini et al. 2015) takes place at higher values of \mathcal{D} (e.g. partial and total disruption from intermediate-mass MBH binary at $\mathcal{D} > 5$ and > 15 Khan & Holley-Bockelmann 2021). Taking into account the above and motivated by the observations of local NSC (Neumayer & Walcher 2012), we select conservatively $\mathcal{D}_{\text{nuc}} = 0.1$. We stress that this parameter (along with $M_{*,\text{NSCcut-off}}$) can be later substituted from a physically motivated formulation when the NSC model is implemented in L-Galaxies by Hoyer et al. (in prep).

We have checked that variations within an order of magnitude of the thresholds mentioned above do not significantly affect the results on the volumetric rates presented in this work. In Sect. 4.4 we investigate the role of the resetting frequency in our results. Specifically, we will assume the extreme case where the TDE resetting occurs only at major mergers and massive disk instabilities and we will use the alternative value of $\mathcal{D}_{\text{nuc}} = 1$.

2.3.3. Treatment of TDEs in AGNs

In the model, many MBHs shine as active galactic nuclei (AGN) until $z = 0$, while at the same time, they are disrupting stars. However, the two processes may not be completely unrelated to each other. For instance, it has been proposed that TDE rates can be enhanced due to the alignment of retrograde orbits of NSC stars with the MBH accretion disk (Generozov & Perets 2023; Nasim et al. 2023) or due to the turn-off of an AGN disk (Wang et al. 2024). However, by construction, our model does not account for such possible rate enhancement since gas physics are not included in PHASEFLOW. Regarding the impact of TDEs on the AGN disk, the few TDE interpretations of fast flares in AGN light curves suggest a (temporal) post-flare increase (Blanchard

et al. 2017; Liu et al. 2020) and others a decrease (Cannizzaro et al. 2022; Cao et al. 2023) of the AGN luminosity. Given the high uncertainty, we assume that the disk recovers quickly (compared to the time for the next TDE) or is not interrupted at all by TDEs so that both the TDE and AGN luminosity are kept as independent properties of each MBH. Given the unconstrained physics of the TDE and AGN interactions mentioned above, our results should be considered as an indicative prediction of the incidence rate of TDEs in active MBHs. We do not expect this assumption to affect the global rates a lot due to the small AGN fraction at $z \sim 0$ ($< 10\%$ of MBHs are active) unless the TDE rates are significantly boosted in the presence of an accretion disk (by a factor of 10 or greater).

2.3.4. From simulated to observable TDE rates

Once TDEs are carefully linked to the MBHs and their galaxies evolving within L-Galaxies, we need to transform the individual rates to observable events to finally compare our predictions with the events picked up by time-domain surveys. Here we keep the following minimum number of assumptions to translate simulated TDE rates to observed ones:

- Given the resolution of our simulation and the multidimensional grid we use, we omit from the analysis the TDE rates from galaxies with masses $M_* < 10^{5.5} M_{\odot}$ and/or MBHs $M_{\bullet} < 10^{2.5} M_{\odot}$.
- Regarding the orbits of individual stars, we suppose that all black holes of the same mass and spin experience the same TDE (given the mass of a star). In reality, for massive stars only those with a pericenter that is a fraction of the tidal radius are fully disrupted (otherwise they are partial), and the energy output of the events may depend on the penetration factor of the star. Moreover, provided that a handful of partial disruption events have been identified (Payne et al. 2021; Malyali et al. 2023), we discuss the impact of such a choice in Sect. 5.
- Given the output TDE rates of an MBH, we can decide if these are going to contribute to the bulk TDE rates or not, due to the event-horizon suppression. We consider this to depend only on the following assumptions; a) the stellar mass m_* of the disrupted star, which we draw from a truncated Kroupa function ($m_* < 1.5 M_{\odot}$), b) the age of the loss-cone since the cluster/galaxy component last reset $\Delta t_{\text{TD,i}}$ and c) the spin parameter of the black hole χ_{\bullet} . The last two are outputs of L-Galaxies. We draw the Hills mass $M_{\bullet,\text{max}}(m_*, \Delta t_{\text{TD,i}}, \chi_{\bullet})$ from the tabulated results of Huang & Lu (2024, Table D1) which have performed various simulations of solar-metallicity stars disrupted by MBHs.¹² If $M_{\bullet} > M_{\bullet,\text{max}}$, we omit this MBH from the sum of the bulk rates. Otherwise, we assume that all events are full TDEs and have the rate assigned to the MBH.¹³
- We assume that all full tidal disruption events will be detected (note that the observational constraints are corrected

¹² These authors may have used slightly different environmental setups, but we expect the values to be quantitatively close.

¹³ From theory, e.g. MacLeod et al. (2012) and Kochanek (2016), for a given M_{\bullet} , TDE rates scale with the initial mass function dN/dm_* and power-law $m_*^{1/6}$. This will matter mostly beyond the maximum Hills mass for $m_* = 0.38 M_{\odot}$ ($M_{\bullet} > 10^8 M_{\odot}$), a mass range that TDE rates are shown only indicatively. Although the dependence on the initial mass function is captured with the sampling of stars, we do not rescale rates with this power-law dependence for massive monochromatic stars when adding them to the bulk rates.

¹¹ Note that this choice is somehow arbitrary and it guarantees the MBH does not move by more than three bins away in the grid of rates, compared to where it should be.

for completeness, but not for obscuration and line-of-sight effects) if there is no AGN contribution. In the presence of an AGN, we ignore TDEs in MBHs with AGN bolometric luminosity $L_{\text{bol}} > 10^{42} \text{ erg/s}$ (*fiducial* model) unless noted otherwise.

3. Results

In this section, we present our main results regarding the comparison of our model predictions for the *fiducial* choice of parameters with the TDE rates observed by the latest time-domain campaigns. We also discuss the implications of our model for the time evolution of TDE rates and the general properties of the MBHs and galaxies hosting TDEs. The interpretation of the results in view of the population of NSCs and MBHs, the implications for MBH spin and growth through TDEs is later discussed in Sect. 4.

3.1. Volumetric TDE rates

In Fig. 5, we present our predictions for the volumetric rates as a function of MBH and galaxy stellar mass for our *fiducial* model and we compare them with the recent constraints reported in Yao et al. (2023) by making use of a sample of 33 TDEs from the ZTF survey. As shown in the left panel of Fig. 5, our model can reproduce the overall normalization of the volumetric rates and, at $M_{\bullet} > 10^{6.5} M_{\odot}$ we find the declining shape of the observed volumetric rates. In addition, Yao et al. (2023) also derived a simple model for the volumetric rates as a function of MBH mass using the Gallo & Sesana (2019) and Shankar et al. (2016) mass functions and including event-horizon suppression (dotted-dashed lines in the left panel of the figure), and our predictions are in overall agreement with these models.

The primary discrepancy between our predictions and the aforementioned observational results is at $M_{\bullet} < 10^{6.5} M_{\odot}$ where we find a declining trend. On one side, in our model, the turnover in the low-mass regime is due to lower average NSC masses and greater ages around small MBHs (which translates into significantly reduced TDE rates by $z=0$). On the other side, Yao et al. (2023) assign to the detected events black hole masses based on the $M_{\bullet}-\sigma_{*}$ relation from (Kormendy & Ho 2013), which can lead to an underestimation of the real MBH masses (e.g. an alternative scaling for inactive MBHs Reines & Volonteri 2015). Moreover, one of the dimmest events of (Yao et al. 2023), AT2020vdc with an assigned mass of $M_{\bullet} \sim 10^{5.5} M_{\odot}$, has recently been flagged as a partial disruption (Somalwar et al. 2023a), a class of events that is not included in our predictions.

Our results are also broadly in agreement with the volumetric rates as a function of MBH derived from the eROSITA X-ray luminosity function assuming an Eddington-limited accretion and a simple volumetric correction¹⁴ of $k_{\text{bol}} = 15$. The two classes of optical-UV and X-ray TDEs might not be eventually different as inferred from recent studies (Guolo et al. 2023), so we anticipate the two mass functions to be similar (which is the case within errors with the simple transformation we performed). Finally, in the left panel of Fig. 5 we also plot the previous constraints from van Velzen (2018) for reference. These are higher than both the model predictions and the Yao et al. (2023) constraints at all MBH masses below event-horizon suppression. This could be

due to the smaller number of statistics (17 TDEs) and the heterogeneous nature of the van Velzen (2018) sample (see discussion for the low-end of the luminosity function, Yao et al. 2023).

In the right panel of Fig. 5 we present the model results about the volumetric rates as a function of the host-galaxy stellar mass, M_{*} . As shown, our predictions at $z=0$ display a broad agreement with the shape of the distribution from Yao et al. (2023). We note that the difference in the normalization could be alleviated by increasing the MBH and/or the NSC occupation fraction or allowing larger NSC masses in the model (as discussed in Sect. 4.2 & Sect. 4.4).

To describe the distribution of observed TDEs, Yao et al. (2023) derive a model using the galaxy stellar mass function coupled with a power-law dependence of the rates on galaxy mass ($M_{*}^{-0.4}$, originally from the rate dependence on MBH mass M_{\bullet}^B with $B = -0.25$). A similar functional form has been used previously, e.g., for various local galaxies (Wang & Merritt 2004), and for galaxy central cores and cusps (Stone & Metzger 2016). At the range $M_{*} = 10^{9.5} - 10^{10.5} M_{\odot}$ our model prediction can be fitted with a similar power-law, but we predict a different functional form at the low mass end.

3.2. Per-galaxy TDE rates

In Fig. 6, we show the per-galaxy TDE rates as a function of MBH mass (left panel) and stellar mass of galaxies hosting an MBH (right panel). We further split the contributions to the total TDE rates from NSCs and the galaxy component¹⁵, further subdivided into old ($\Delta t_{\text{TD}} > 10 \text{ Gyr}$) and young ($\Delta t_{\text{TD}} < 100 \text{ Myr}$) systems. We immediately see that the contribution of NSCs to the total rates reaches higher values across all masses. The galaxy component rates increase both with MBH and galaxy mass up to the event-horizon suppression mass. However, they are on average *more than three orders of magnitude* lower when compared to the contribution from the NSC at MBH/host galaxies of the same mass. This result has important implications for the expected nucleation fraction of galaxies, which we will further discuss in Sect. 4.2. Indeed, based on these results, *TDEs should be predominately observed in the presence of NSCs*. Current observations of TDEs are primarily from distant enough sources where NSCs remain unresolved.

When looking at the difference between “old” and “young” systems, we see a different behavior for the NSCs and the galaxy contributions. Recently formed NSCs give the highest contributions to the per-galaxy rates, with approximately constant values of $\sim 10^{-5} \text{ yr}^{-1}$ per MBH/galaxy (see bottom panel of Fig. 3). Instead, older systems below $M_{\bullet} < 10^7 M_{\odot}$ exhibit a power-law dependence on MBH mass, namely $\dot{N}_{\text{per-MBH}} \propto M_{\bullet}^B$ with $B = 1$ (compared to $B = 0$ for young systems under the same definition). The “old” NSCs have on average small mass compared to their MBH (the majority of galaxies have $M_{\text{NSC}} < M_{\bullet}$). For these systems, the relaxation time becomes significantly short, thus the loss cone gets quickly depleted. At the low mass regime, the majority of systems have “old” rather than “young” rates (the median value of assigned TDE rates is close to the light-colored dotted line). This has specific implications for the dwarf galaxy regime (yet to be probed with observations), where per-MBH/per-galaxy TDE rates are higher by a factor of >10 for young NSCs over older NSCs. Therefore, our work suggests that a promising opportunity of sampling TDEs is selecting re-

¹⁴ computed simply as $M_{\bullet}[M_{\odot}] = k_{\text{bol}} L_X / L_{\text{edd},1}$ where $L_{\text{edd},1}$ the Eddington luminosity for a solar-mass compact object and L_X the soft X-ray luminosity

¹⁵ As mentioned in the model description, the galaxy component contributing to TDEs is assumed to be the bulge, or the disk in the absence of bulge.

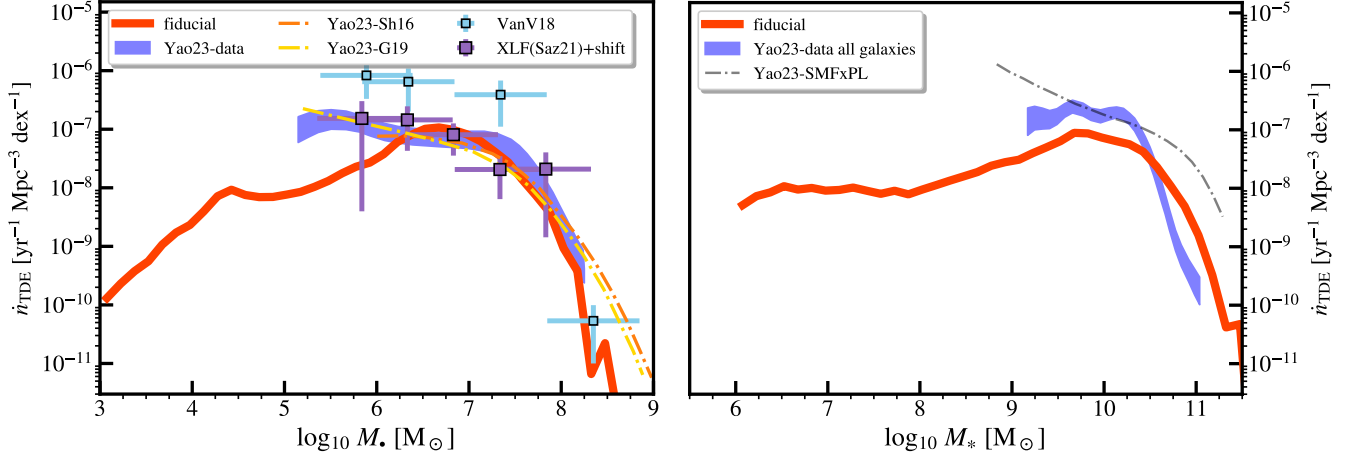


Fig. 5. Volumetric TDE rates per black hole (M_{\bullet} , left) and galaxy (M_* , right) log mass at $z=0.0$ for the *fiducial* model (solid line). Our model is compared against the constraints (here plotted with the error range) from Yao et al. (2023) for all MBHs (left) and all galaxy types (right). For reference, we display the previous constraints from van Velzen (2018) and the luminosity function from Sazonov et al. (2021) transformed to a mass function (see the details in the text). We also display the model lines of Yao et al. (2023) for the TDE rates as a function of a) MBH mass, assuming the Shankar et al. (2016, maroon shorter dash-dotted line; Sh16) and the Gallo & Sesana (2019, cyan long dash-dotted line; G19) MBH mass functions, both including the event-horizon suppression b) galaxy stellar mass, obtained by multiplying the galaxy mass function with the power-law dependence of rates on $M_*^{-0.41}$ (grey dotted-dashed, SMF_{xPL}).

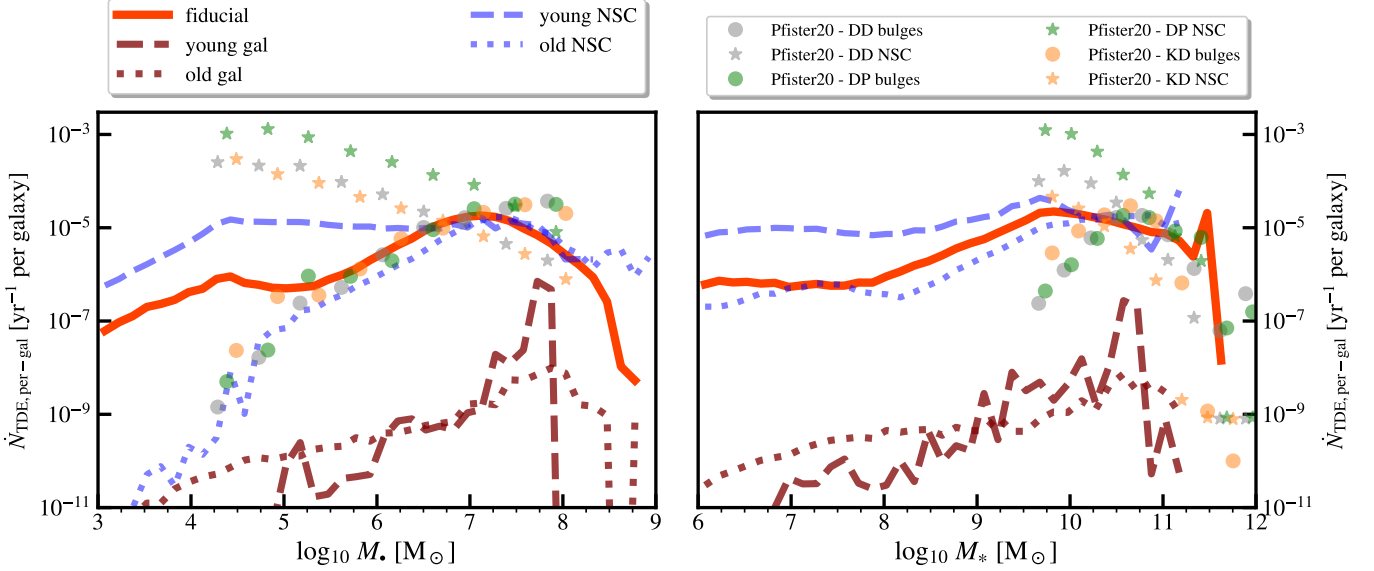


Fig. 6. Average TDE rates per log mass of MBH M_{\bullet} (left) and of MBH-host galaxy M_* (right) for the *fiducial* model at $z=0.0$ (solid red line, tagged as “all”). We average separately over NSC rates (light-blue lines) and galaxy component rates (maroon lines), and subsequently splitting to just restarted (“young” systems with $\Delta t_{\text{TD}} \ll 100$ Myr, dashed line) and after a long time (“old” systems with $\Delta t_{\text{TD}} > 10$ Gyr, dotted lines). For comparison, we present the results of (Pfister et al. 2020) for three different scaling relation pairs of MBH-galaxy mass & NSC mass-size adopted in their work (DD, DP, and KD as defined in Table 2 of Pfister et al. 2020) to bracket the uncertainties following these hypotheses.

cently interacting systems (young, $\Delta t_{\text{TD,gal}} < 100$ Myr), with a predicted per-galaxy (volumetric) rate of $\sim 1 \times 10^{-5} \text{yr}^{-1}$ ($\sim 1 \times 10^{-7} \text{yr}^{-1} \text{Mpc}^{-3} \text{dex}^{-1}$). This prediction holds down to the least massive dwarfs, as marked by the flattening of the rates as a function of galaxy mass (for both per-galaxy and volumetric TDE rates, see respectively the right panels of Figs. 5 and 6). This revision of rates in dwarf galaxies may have a significant impact on theoretical predictions of TDEs in intermediate-mass MBHs. The galaxy contribution shows a different behavior with age. First of all, we note again that TDEs from the galaxy component do not strongly depend on time and that bulges lead to larger rates compared to pure disks (see discussion of Fig. 3 in

Sect. 2.2). In Fig. 6, we see that old systems have higher per-galaxy rates concerning the young galactic components at the lower MBH $M_{\bullet} < 10^{6.5} M_{\odot}$ and galaxy $M_* < 10^9 M_{\odot}$ masses. We attribute this to the morphological differences between old and young galaxies in this mass range: L-Galaxies predicts that young systems are mostly pure disks (with an average bulge-to-total mass ratio of $\langle B/T \rangle = 0.075$), while old systems are preferentially bulge-dominated ($\langle B/T \rangle = 0.3$). At the high mass end, instead, we see that young galaxies have higher per-galaxy rates than old ones as a function of galaxy mass. In this case, the difference can be attributed to the differences in the $M_{\bullet} - M_{\text{gal}}$ ratio for young and old systems: at fixed galaxy mass as an

effect of early on-set of MBH growth, old systems are preferentially hosting heavier MBHs, whose galaxy-component rates are lower. In both cases the per-MBH rate follows a power-law of the form $\dot{N}_{\text{per-MBH}} \propto M_{\bullet}^B$ with $B \approx 0.7$ for the mass range $M_{\bullet} = 10^6 - 10^8 M_{\odot}$.

Our model predictions in Fig. 6 are then compared with the ones of Pfister et al. (2020) which, motivated by the computation of TDE rates in observed galaxy profiles, computed the per-galaxy TDE rates for a mock catalog of galaxies hosting NSCs and with a well-characterized bulge component. Before making a comparison, it is worth noticing that Pfister et al. (2020) derives MBH masses using, also in the low-mass regime, $M_{\bullet} - M_{*}$ scaling relations observationally derived for massive spheroidal galaxies (Kormendy & Ho 2013; Davis et al. 2019). Moreover, although they use PHASEFLOW to compute the TDE rates, they assume a monochromatic star distribution of $m_{*} = 1 M_{\odot}$, while this work uses $m_{*} = 0.38 M_{\odot}$ and stellar black holes ($16 M_{\odot}$), a difference that can change by a factor of two the number of stars entering the loss cone, thus available for TDEs (Stone & Metzger 2016).

The per-galaxy rates for NSCs (solid red lines) are consistent with the predictions of Pfister et al. (2020) for $M_{\bullet} > 10^{6.5} M_{\odot}$ and $M_{*} > 10^{10} M_{\odot}$ but have a different trend (they diverge) at lower masses. We suspect that the main difference to the rates towards lower masses is the use of steep Sérsic profiles n_{NSC} for low mass NSCs, using the scaling relation of Pechetti et al. (2020) (for $M_{\text{NSC}} < 10^6 M_{\odot}$ the relation gives Sérsic indices with values above 4). This anti-correlation for NSC indices at lower masses appears to be weaker in the recent results of Hoyer et al. (2023). We instead assume shallower, possibly more realistic, profiles, as described in Sect. 2.2 and no correlation of the steepness of the profile with mass. Moreover, Pfister et al. (2020) do not allow for small structures with $M_{\bullet} > M_{\text{NSC}}$, while there is evidence of such objects and they are naturally included in our model (see Sect. 4.4 for the impact of this parameter).

Regarding the TDE rates from the galaxy component, Pfister et al. (2020) also finds an increase both with MBH and galaxy mass until the event-horizon suppression mass. Nevertheless, the average rate they predict is three to four orders of magnitude higher than our predictions for all galaxy mass ranges. This is probably because Pfister et al. (2020) assumes on average more centrally concentrated galaxies compared to our work. Also, as mentioned earlier, at the low galaxy stellar mass end, they assign MBH masses using the same steep relation as for a more massive system: this implies that, at fixed MBH mass, their stellar mass can be up to two dex larger than ours.

The results just discussed highlight that the demographical analysis of TDE rates requires a realistic cosmological environment with carefully constructed morphological galaxy properties and number distributions as a function of galaxy mass, as provided by L-Galaxies.

3.2.1. Redshift evolution of TDE rates

Having captured the $z=0$ global rates, we now discuss their redshift evolution and how that compares with the evolution of the underlying MBH properties and their environment.

In Fig. 7 we display the volumetric TDE rates for redshifts $z = 0, 1, 2$. Regarding the case of TDE rates as a function of MBH mass, there does not seem to be a significant change in the rates between $z=0$ and $z=1$. This is caused by the fact that the model predicts a very mild MBH evolution at $z < 1$, and thus the black hole mass function remains almost unchanged. This trend

differs from the constant increase of rates for all MBH mass ranges from high redshift down to $z=0$, proposed by Kochanek (2016), but it is aligned with the usual assumption that the volumetric TDE rates do not evolve significantly with redshift (see e.g. van Velzen & Farrar 2014; van Velzen 2018; Yao et al. 2023). Despite this, there is a slight decrease of half an order of magnitude when comparing resolved TDEs at $z=0, 1$ and $z=2$, which will be an important feature to study in future studies with deep sky surveys such as LSST (Hambleton et al. 2023; Bricman & Gomboc 2020; Bučar Bricman et al. 2023) and UV transient surveys like QUVIK (Zajaček et al. 2023). However, it is worth mentioning that our predictions are model-dependent. We assume that MBHs are hosted by NSCs at all times with 100% probability (see Sect. 2.1.2). For example, if this probability is lower, and NSCs assembly as galaxies and MBHs merge together, then there would be a moderate evolution from $z=2$ to $z=0$, because of the increase of the probability of an MBH being hosted by NSC.

The volumetric rates shown in Fig. 7 can be divided into contributions from the galaxy component (“gal”) and the NSC. The first, although it steadily increases from $z=2$ to $z=0$ with the increase of bulges in galaxies, still provides a negligible contribution to the volumetric TDE rates at all masses and all redshifts. In practice, the volumetric rate is entirely due to galaxies hosting NSCs. This contribution is not shown in the figure as it essentially coincides with the total volumetric TDE rates (“fiducial”). While the per-galaxy rates for NSCs remain the same at high masses towards higher redshifts, there is a slight enhancement (factor less than three) compared to $z=0$ for $M_{\bullet} < 10^6 M_{\odot}$ MBH and $M_{*} < 10^9 M_{\odot}$ host-galaxy masses, because of continuous reset of TDE rates during frequent mergers at cosmic noon. This somewhat counteracts the decrease of the number density of inactive MBHs towards higher redshifts and results in a moderate evolution of the volumetric TDE rates.

3.3. TDE rates in active MBHs

Searches for TDEs in AGN at optical (Dgany et al. 2023, ZTF) and X-ray (Homan et al. 2023, eROSITA) wavelengths have not yielded many representative cases. However, observations of luminous ambiguous nuclear transients (Frederick et al. 2021; Hinkle et al. 2022; Oates et al. 2023), TDEs and TDE-like flares in ongoing/previous AGN (Li et al. 2023; Huang et al. 2023; Makrygianni et al. 2023; Charalampopoulos et al. 2024), and changing-look AGN (Ricci & Trakhtenbrot 2023; XueGuang 2022) hint that the two TDE and AGN activity could be related. So far, few theoretical works (Karas & Šubr 2007; Chan et al. 2019; McKernan et al. 2022; Prasad et al. 2023) and recent simulations (Ryu et al. 2023b) have explored the co-existence of TDEs and AGN. Predicting TDEs in AGN hosts is beyond the scope of this paper, as it requires dedicated modeling of the electromagnetic emission of individual events, considering the relative brightness of TDEs and their host. This section overviews TDE occurrence in AGN under the assumptions outlined in Sect. 2.3.3, aiding future searches for transient events in AGN.

In Fig. 7 we show the volumetric global rates at $z=0, 1$ and 2 , for MBHs triggering AGN with *low*, *moderate* and *high* bolometric luminosity bins: $\log_{10}(L_{\text{bol}} [\text{erg/s}]) \in [39.0, 40.5]$, $[40.5, 42.0]$ and $[42.0, 45.0]$. Note that for *high* AGN luminosity, the detectable rate of events will depend on the luminosity of individual TDEs. In other words, only TDEs with peak luminosity significantly higher than the AGN luminosity at a given wavelength would allow distinguishing the characteristic time-

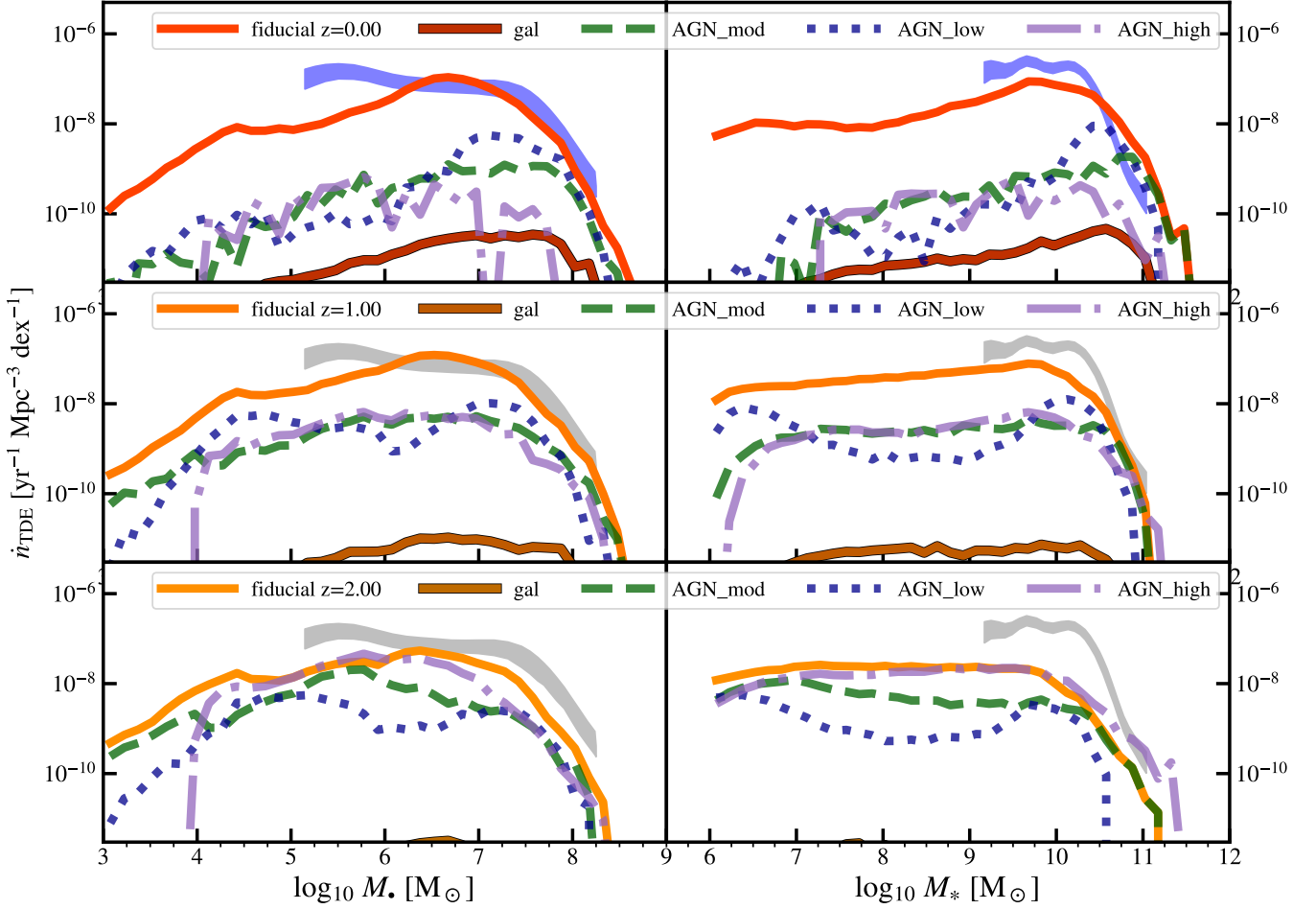


Fig. 7. Redshift evolution [$z=0$ (top), $z=1$ (middle), $z=2$ (bottom)] of the volumetric TDE rates per MBH (left) and stellar (right) mass originating from *all* low-luminosity or inactive MBHs (cut-off at $\log_{10} L_{\text{AGN}} [\text{erg/s}] < 42$ for the *fiducial* model, solid lines) and TDE rates from the galaxy components only (bulges/disks; solid lines tagged as “gal”). We also display the rates only from AGN-hosts with *high* (purple dashed-dotted), *moderate* (green dashed), and *low* (blue dotted) luminosity ($\log_{10} L_{\text{AGN}} [\text{erg/s}] \in [42, 45]$, $[40.5, 42]$ and $[39, 40.5]$ respectively). The $z=0$ constraints Yao et al. (2023) are plotted in all panels for reference (with grey when they do not apply). These fractions remain qualitatively the same for these redshifts for most of the parameter variations.

decay of a TDE light curve, thus singling out the event from AGN stochastic variability or unrelated flaring activity. The first thing to notice in Fig. 7 is that the strong redshift evolution of the AGN luminosity function leaves an imprint on the AGN hosting TDEs. Indeed, the lower the redshift, the greater the importance of inactive MBHs in the volumetric TDE rates. This is because a large fraction of massive black holes consume their high- z gas reservoir and end up in an inactive phase in the low- z Universe.

We observe that at high MBH and host-galaxy masses ($M_{\bullet} > 10^8 M_{\odot}$ and $M_{\ast} > 10^{10.5} M_{\odot}$) and at all redshifts, the volumetric rate of TDEs occurring in luminous AGN (all luminosity bins) is comparable to the one occurring in inactive or low activity AGN (*fiducial*) curve and almost redshift-independent at values $1\text{--}3 \text{ Gpc}^{-3} \text{ yr}^{-1} \text{ dex}^{-1}$. Specifically for redshift $z=2$, the TDE rates of luminous AGN (*high*) dominate over the rates of low-activity MBHs at all host-galaxy masses and $M_{\bullet} < 10^{6.5} M_{\odot}$ MBHs. Therefore monitoring flares in AGN at $z > 1$ might be an effective way to identify TDEs, assuming that a significant fraction of TDEs will be brighter than the AGN emission itself.

4. Discussion

Here we address the implications of the inclusion of TDEs for the modeling of MBHs with L-Galaxies, and explore how the results presented in this work are affected by the parameters and assumptions of our model (Section 2).

4.1. MBH growth via Tidal Disruption Events

As mentioned in the Introduction, the role of TDEs in the mass content of MBHs has been so far theoretical, with no means to calibrate this mechanism at analytical prescriptions of this MBH growth channel. Since our work already is in broad agreement with the TDE rates at $z=0$, we can draw some first conclusions on the contribution of TDE rates to the growth of the MBH population. Here we limit the discussion to the impact of TDE on the growth of the MBH population by $z=0$. A more detailed investigation of the conditions for efficient growth via TDEs and of the sub-categories of galaxy types where this growth channel is important will be the subject of follow-up work (Polkas et al. in prep).

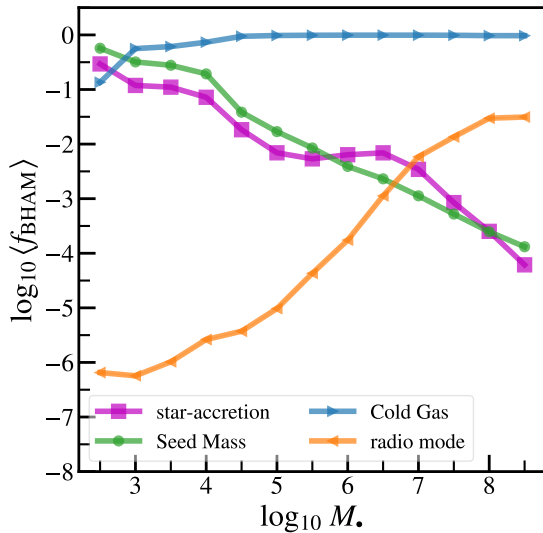


Fig. 8. Average fraction of mass accreted by different MBHs at $z=0$ (f_{BHAM}) via stellar captures (purple squares), cold gas accretion (blue right triangles), hot gas accretion (orange left triangles) and accumulated seed mass (green circles).

In Fig. 8, we show the fractional cumulative mass content of MBHs, namely f_{BHAM} ¹⁶ at $z=0$ as a function of their mass. As demonstrated, the mass growth through TDEs is mostly insignificant for the high mass ranges (i.e. $f_{\text{BHAM}} < 1\%$ for $M_* > 10^5 M_\odot$), especially when compared to the mass growth induced by cold gas accretion. However, for MBHs that remain close to their seed mass $M_* = 10^{2.5} - 10^5 M_\odot$, TDEs offer a competitive channel of growth, composing $f_{\text{BHAM}} = 1 - 10\%$ of their mass. Notably, for the lightest mass bin $M_* < 10^3 M_\odot$, TDE growth is as important as the cold gas accretion, the later being less significant (if at all existent) in dwarf galaxies (see Fig. 7 and Fig. 10 of Izquierdo-Villalba et al. 2019; Spinoso et al. 2023, respectively). For the relative massive MBHs at $z=0$ ($M_* > 10^6 M_\odot$), their seeds grow through gas accretion to $M_* = 10^4 - 10^6 M_\odot$ by $z=2-3$, allowing for important cumulative TDE growth (after the initial gas growth) until $z=0$. This is shown by the *bump* which brings the star-accretion curve over the seed mass one (for MBHs with $M_* = 10^6 - 10^{7.5} M_\odot$). Both M_* and M_{NSC} will be greater for MBHs of this mass range, resulting in constant high rates with time compared to those of surviving dormant seeds living in isolation. The later cannot maintain a constant high rate as indicated by the per-MBH rates for old NSC systems in Fig. 6. More massive MBHs ($M_* \sim 10^8 M_\odot$) form early at the most massive galaxies ($M_* \sim 10^{11} M_\odot$) of the simulation which will stop hosting NSCs earlier and grow less their MBH through TDEs.

Our results add realism to estimates from earlier works. Unlike claims using the full loss-cone theory (e.g. Milosavljević et al. 2006; Alexander & Bar-Or 2017), the growth via TDEs in our model is not such that all $M_* < 10^4 M_\odot$ MBHs would reach the supermassive regime as a result of stellar accretion. We attribute this behavior to a) the vast majority of low-mass MBHs being hosted in lower-mass galaxies with less massive NSCs and b) the time-dependent nature of the rates; non-interacting ancient NSCs relax quickly and can even become less important than the bulge/disk rates (see input rates Fig. 3). As mentioned above,

¹⁶ Here, the definition of the total black hole accreted mass (BHAM) includes the mass content in seed mass, although strictly speaking, this is not accreted onto the MBH.

however, we will study in a follow-up work the specific properties of the environment and redshifts that lead to more efficient growth via TDEs.

4.2. Implications for MBH and NSC populations

Complete galaxy samples are starting to constrain the AGN occupation fraction across different galaxy masses, hinting at significantly smaller AGN fractions in dwarf galaxies (i.e. $< 10^{-2}$) than in massive systems (see e.g. Mezcuca et al. 2018; Mezcuca & Domínguez Sánchez 2020; Bykov et al. 2023; Zou et al. 2023; Siudek et al. 2023). This could be explained if the number of AGN in dwarf galaxies remains small because of the lack of cold gas at the center of these systems (Urquhart et al. 2022) which cannot sustain significant MBH growth. Therefore, AGN cannot be used as good tracers of low-mass MBHs (nor of the full population of MBHs). Alternatively, the abundance of MBHs in the local universe and beyond can be unveiled by exploiting the population of TDEs in all-sky transient surveys.

As shown in Section 2.1.1 and Section 2.1.2 our *fiducial* model is in fair agreement with both the MBH mass function and the NSC occupation fraction. However, there are uncertainties at the low-mass end of the MBH mass function and the frequency of MBHs hosted by NSCs is currently unknown. To address these uncertainties, we compare our *fiducial* model to a run with the highest number of MBHs permitted by our model, hereafter *maxOcc* model. They differ in the amplitude of the MBH seeding probability,

$$G_p = 0.25 \text{ (fiducial) vs } 1.0 \text{ (maxOcc)},$$

resulting in different MBH occupation fractions of $M_* > 10^5 M_\odot$ at $z=0$, as shown in the top panel of Fig. 9. The large occupation fraction of MBHs¹⁷ in galaxies has a direct effect on the abundance of NSC. Specifically, the *maxOcc* model displays an NSC occupation up to a factor 1.6 larger than the one shown in the *fiducial* case, as reported in the central panel of Fig. 9.

The bottom panel of Fig. 9 shows that the changes in the MBH and NSC occupation result in appreciable differences in the observed TDE rates per galaxy. Specifically, the *maxOcc* shows a better agreement with the results of Yao et al. (2023). Despite this improvement, the *maxOcc* model is still incompatible with the recent interpretation of Yao et al. (2023) which suggests a flat (or slightly positive) power-law shape of the MBH mass function at $M_* < 10^7 M_\odot$. Quantitatively, both of our models suggest: $p \lesssim -1$ for $dn_*/d \log_{10} M_* \propto M_*^p$, instead of $p \gtrsim 0$, as found by Yao et al. 2023. Also, both the *maxOcc* and *fiducial* models support the interpretation of van Velzen (2018) for a flat ($\sim 100\%$) occupation fraction of MBHs down to $M_* \sim 10^{10} M_\odot$. However, they differ in the dwarf galaxy regime ($M_* = 10^7 - 10^{9.5} M_\odot$ at middle panel of Fig. 9). This higher occupation is the main driver in boosting the volumetric TDEs at all galaxy stellar masses.

Regarding the NSC occupation, the *fiducial* model matches the observations of Virgo (and Fornax at lower masses) clusters (Muñoz et al. 2015; Eigenthaler et al. 2018; Sánchez-Janssen et al. 2019), while the *maxOcc* resembles the higher NSC occupation in the Coma cluster (den Brok et al. 2014; Zanatta

¹⁷ For the sake of brevity, we do not show the black hole mass function of the *maxOcc* model. This model tends to overpredict by a factor of three the number of MBHs in the mass range $M_* = 10^6 - 10^{7.5} M_\odot$, compared to observational constraints at $z=0$ from Shankar et al. (2009). Besides this, the overall shape of the mass function remains relatively similar concerning the *fiducial* model at high masses.

et al. 2021). Most of the clusters in our model are less massive than their MBH mass (see Appendix A for mass distribution of NSCs). In particular, only $\approx 30\%$ and 60% of MBHs, hosted in galaxies with mass $M_* \sim 10^7 M_\odot$ and $10^{9.5} M_\odot$ at $z=0$, are also found in an NSC more massive than them, namely $\mathcal{D} = M_{\text{NSC}}/M_* > 1$. For reference, the median mass ratio between NSCs and their associated MBHs with a measured mass is $\mathcal{D} \sim 4$ (Greene et al. 2020), although detections are made in the most massive systems hosting MBHs $M_* > 10^6 M_\odot$.

We underline that there is a degeneracy between the occupation of MBHs per galaxy and the occupation of NSCs per MBH. In particular, simultaneous increase and decrease of each number density can result in the same observed normalization of the volumetric TDE rates. Yet, the better agreement of the *maxOcc* model with observations indicates that MBH and NSC occupation fractions should be on average skewed towards the highest values of the respective $z \sim 0$ observational constraints. Interestingly, denser environments (galaxy clusters) are found to have higher-than-average occupation fractions of both MBHs (Tremmel et al. 2023) and NSCs (Sánchez-Janssen et al. 2019; Hoyer et al. 2021; Zanatta et al. 2021; Leaman & van de Ven 2022) at a given galaxy stellar mass, in line with *maxOcc* model predictions. Based on our model and the novel TDE rates per-galaxy of our study we speculate that the following conditions should be fulfilled by future models, for them to explain the observed TDE rates: i) a tight connection between the two families of nuclear compact objects (in our model all NSCs host an MBH) and ii) the dominant contributor to TDE rates to be MBHs hosted in $M_* \sim 10^9 - 10^{10.5} M_\odot$ galaxies in dense environments, where NSC and MBH occupation reach 100% and the per-galaxy rate is peaking. An explicit study of the environment dependence, involving realistic star clusters and NSC modeling will be needed to further understand the connection between the two classes of objects.

4.3. Spin Evolution & Implications for TDE rates

MBHs close to the Hills mass ($M_* \sim 10^8 M_\odot$) should exhibit near-to-zero TDEs by $z=0$, and if they do they should be spinning (Kesden 2012). Also, because of their rarity, any TDE observed at this mass range will reside statistically at higher redshift (van Velzen 2018; Mummery & Balbus 2020; Hammerstein et al. 2023). Still, with the handful of massive systems observed with TDEs in the ZTF sample (Yao et al. 2023) we can test large volume statistics of the model’s MBH spin distribution.

As shown in Sect. 2.1, L-Galaxies predicts a median spin of $\chi_* \sim 0.6$ for MBH with masses $M_* > 10^7 M_\odot$. Note that when initially applied on the lower-resolution *Millennium-I* simulation (Izquierdo-Villalba et al. 2020), the spin model predicts that $M_* \lesssim 10^8 M_\odot$ MBHs remain high-spinning ($\chi_* > 0.8$) down to $z \sim 0.1$. Overall, the agreement¹⁸ of the predicted volumetric rates at high MBH masses with observations (Fig. 5) suggests that the model makes a reasonable prediction of the spin distribution at $z < 0.5$.

To guide the reader and bracket the effect of the spin model on the event-horizon suppression, Fig. 10 displays the volumetric TDEs for the same MBH population of the *fiducial* model but assuming $\chi_* = 0$ and $\chi_* = 0.998$ when computing the event horizon suppression (Sect. 2.3.4) as a shaded region around the model line. As shown, a non-spinning MBH population at the

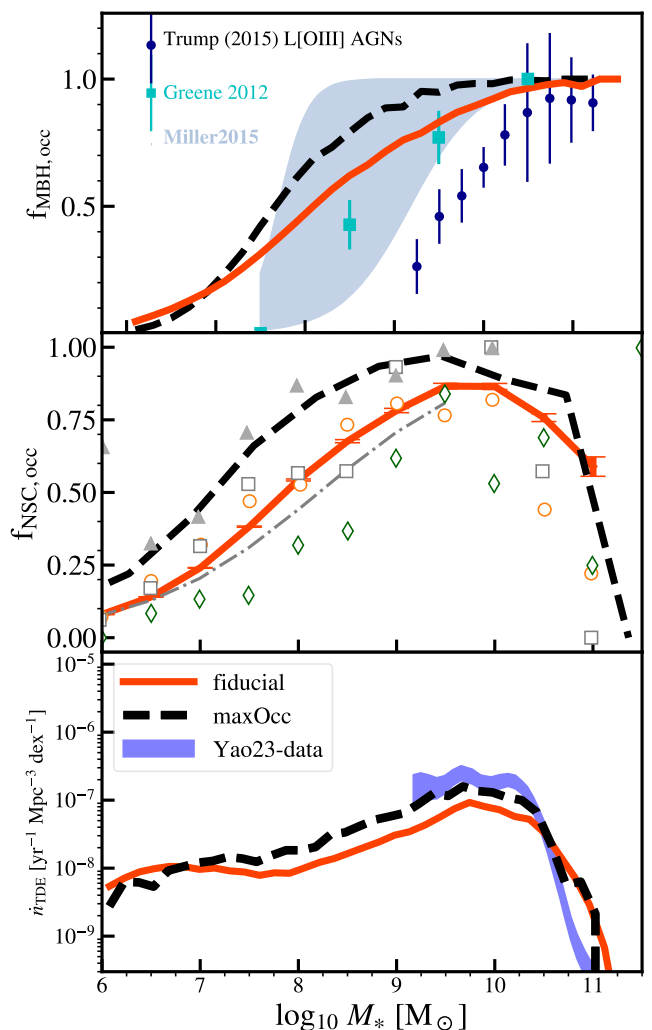


Fig. 9. Top and middle panels: occupation fractions of MBH ($M_* > 10^5 M_\odot$, top) and NSC (all masses, middle) that result into the volumetric TDE rates as a function of galaxy-host mass (bottom). We show the *maxNSC* and *maxOcc* models with orange solid and black dashed lines, respectively. In the top panels we display the local MBH occupation fraction derived from a compilation of detections Greene (2012, cyan squares) and X-ray constraints by Miller & Davies (2012, light-blue region), as well as an occupation for slightly higher redshifts $0.01 < z < 0.1$ derived via optical-line AGN (Trump et al. 2015, blue circles). In the middle panel, the data points and logistic function (the dashed-dotted thin line), both from Hoyer et al. (2021), have the same meaning as in Fig. 2. The enhanced MBH occupation is still compatible with the observations of the Coma Cluster (grey triangles), even though it yields a greater fraction of nucleated galaxies. We stress that all NSCs are hosting an MBH in our model, hence adding NSCs without MBHs would increase this fraction. Bottom panel: the *maxOcc* model (dashed line) reproduces better the TDE-rate distribution constraint of Yao et al. (2023) than the *fiducial* model (solid line). The results suggest that a rather high occupation of black holes and NSCs is preferred to explain TDEs at the observed galaxy masses.

mass range $M_* = 10^7 - 10^{8.5} M_\odot$ (left border of the shaded region) can be excluded while a maximally spinning population in the same range, the model rates lie within the error margins of the constraints. Our results are consistent with the recent findings from Mummery et al. (2024) who derived MBH spin $\chi_* = 0.3 - 0.75$ by modeling their late-time TDE emission for 10 MBHs with mass $M_* > 10^7 M_\odot$.

¹⁸ We stress that we have identified the slight underprediction to be due to the lack of massive NSC abundance by the model as discussed in our results (see Sect. 4.4, model tagged as *noMstcut*).

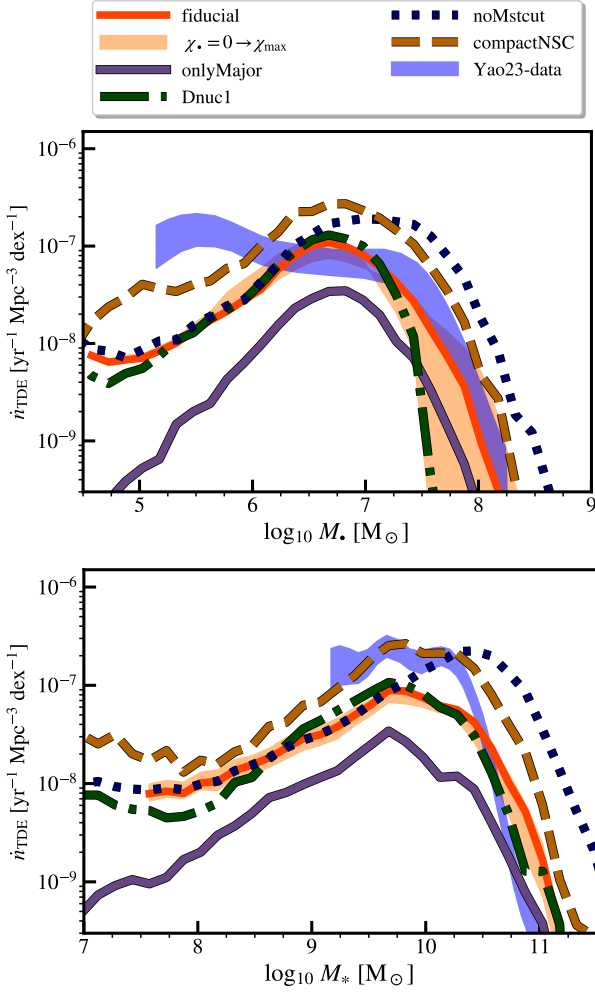


Fig. 10. Volumetric rates at $z=0$ per black hole mass (*top*) and galaxy stellar mass (*bottom*) for different model variations (names of the models in legend as in text), compared with constraints from Yao et al. (2023, blue shaded area) and the *fiducial* model (red solid line). The shaded orange area is constructed by assuming no spin and maximally spinning MBHs in the post-processing treatment of the event-horizon suppression of the *fiducial* model (orange solid line).

We are careful with our interpretation since for converting simulated TDE rates to observable ones we have neglected some aspects of the disruption of the stars themselves. For example, we have used a truncated ($m_* < 1.5 M_\odot$) Kroupa IMF for the event-horizon suppression calculations. Nevertheless, the scenario of a *top-heavy* initial stellar mass functions for the stellar nuclear environment is frequently referenced as an alternative to high-spinning MBHs (Mockler et al. 2022). Our results may also be affected by the distribution of the stellar orbit inclinations as recently indicated by Singh & Kesden (2023). Furthermore, the effects of the De Sitter precession of the streams of the disrupted star on the outcome of a TDE may play an important role¹⁹ (stream self-crossing becomes ineffective Bonnerot et al. 2022; Jankovič et al. 2023, for reference). Nevertheless, our model suggests that basic assumptions for the star population and the detectability of individual events (Sec. 2.3.4), coupled with the spin distribution of L-Galaxies, can fairly reproduce the observed event-horizon suppression.

4.4. The impact of parameters choice

As seen before, the occupation fraction of MBHs in galaxies seems to play an important role in the normalization of the volumetric TDEs, MBH spin distribution regulates the shape at the event horizon suppression. Here, we examine how TDE rates are influenced by other free parameters related to the NSC model (nucleation, regeneration, and compactness) and by the conditions used to reset the TDEs. We highlight that we do not seek to explore the full parameter space but rather pinpoint the most important choices for the model. Also, we stress that our main results for MBH growth do not change qualitatively among runs featuring single-parameter variations.

More compact NSCs. NSCs are the main stellar environments in which TDEs occur (compared to the galaxy contribution, see both per-galaxy & volumetric TDE rates in Fig. 6 and Fig. 7). When computing the number of TDEs of NSCs inside PHASE-Flow we assumed an effective radius of NSCs according to specific scaling relations (see Sect. 2.2). However, a large number of uncertainties are still present in these relations. For example, NSCs hosting an MBH are expected to dynamically evolve (evaporate/expand), so the observed scale radius may be greater than the initial radius (Merritt 2009). Therefore, we have also explored how the compactness of the NSC affects the number of TDEs and consequently, the volumetric TDE rates (hereafter *compactNSC* model). In Fig. 10, we show the volumetric rates for a run where NSCs are initialized with a scale radius a reduced to $1/3$ of what is assumed in our *fiducial* model (see Sect. 2.2.2). This choice is motivated by observations showing NSCs who lie ~ 0.5 dex below the mass-radius relation for NSCs at $z=0$ (see e.g. Pechetti et al. 2020). We observe that the model overpredicts the rates at MBH masses $M_\bullet = 10^6 - 10^{7.5} M_\odot$ by a factor of three, yet it reproduces the volumetric TDE rates as a function of galaxy mass better than the *fiducial* model. The overestimation disfavors NSCs that are significantly more compact than the observed relations used in our *fiducial* model. However, we stress that generating profiles with a one to three-times smaller scale radius can yield better agreement with both TDE mass function on MBH and galaxy mass. We stress that with the current implementation of NSCs, the model lacks the most massive NSCs of mass $M_{\text{NSC}} = 10^8 - 10^9 M_\odot$ which are naturally more compact and will contribute at TDE rates of $M_\bullet > 10^{7.5} M_\odot$ MBH.

Variation of \mathcal{D}_{nuc} . This is a key parameter in our model since it controls the frequency of NSC regeneration. Considering lower values than our *fiducial* case, observations presented in (Neumayer et al. 2020) suggest a value of $\mathcal{D} \equiv M_{\text{NSC}}/M_\bullet$ as low as 0.01. However, it remains unclear if these configurations are just transients. Despite that, we test a value of 0.01, and no significant changes were found. For the sake of brevity and clarity, we do not display the results of this run. Instead, we boost \mathcal{D}_{nuc} towards higher values, from 0.1 to 1 (hereafter *Dnuc1* model) and show our results in Fig. 10. For this case, the rates are heavily suppressed at high MBH mass ($M_\bullet > 10^{7.5} M_\odot$) since the NSCs with values $\mathcal{D}_{\text{nuc}} = 0.1 - 1$ are not nucleated in this run. This is a piece of evidence that small and possibly unresolved NSCs ($\mathcal{D} < 1$) are the main contributors to TDE rates at the event-horizon suppression mass range. However, only the replacement of this parameter with a physical NSC treatment (including the destruction of NSCs) can offer hindsight on why this is the case.

¹⁹ in the scenario where radiation predominantly comes from stream collisions

Variation of cut-off galaxy mass for nucleation. Recently, the careful observational sampling of massive galaxies presented in Ashok et al. (2023) finds a possible higher nucleation fraction in the high-mass end than the one reported in the observational constraints used for this work (i.e. Hoyer et al. 2021). In our phenomenological model of NSCs, we impose a maximum galaxy stellar mass $M_{*,\text{NSC-cutoff}} = 10^{9.75} M_{\odot}$ (Sect. 2.1.2), above which either the conditions are not adequate to trigger the NSC formation or, equivalently, the destruction of NSC becomes important. The specific value of this cut-off is extremely important for $M_* > 10^{11} M_{\odot}$ galaxies since higher values of the cut-off will both allow for a higher number density of NSCs, but also more massive NSCs (since the scaling relation extends to high-mass galaxies). On the other hand, a sufficiently low $M_{*,\text{NSC-cutoff}}$ can turn off the nucleation around $M_* > 10^8 M_{\odot}$ MBHs, converting the galaxy component to the only source of TDEs at this mass range.

To explore how the volumetric rates are affected by the nucleation mass cut-off, in Fig. 10 we present the results of a run where no cut-off is applied, i.e. all galaxies at all masses can host an NSC as long as $\mathcal{D}_{\text{nuc}} > 0.1$ (hereafter, *noMstcut* model). As compared to the *fiducial* model, this parameter variation shows that the inclusion of more massive clusters at more massive galaxies won't affect the low-mass regime of the volumetric rate distribution and increase the rates at the event horizon suppression with error margins. These “more massive” NSCs can be similarly introduced by increasing the scatter on the $M_* - M_{\text{NSC}}$ scaling relation when assigning NSC masses in the model. We anticipate the inclusion of a realistic scenario for NSC evolution and destruction will increase the TDE rates in massive galaxies.

Variation of TDE rates reset frequency. To assess the importance of the conditions used to reset the TDE rates (see Sect. 2.3.2) we consider that only major events are capable of resetting the clock of TDEs ($\Delta t_{\text{TDE},i}$). In particular, major events refer here to (i) major galaxy mergers (satellite/central baryonic mass ratio $> 10\%$) and (ii) disk instability events that displace more than $> 10\%$ of the stellar disk mass to the bulge. Hereafter, we refer to this model as *OnlyMajor* and we present its volumetric TDE rates in Fig. 10. Overall, the predictions of the model are ~ 1 dex below the current observational constraints regardless of the MBH and galaxy masses. Yet, the suppression of rates induced by the *OnlyMajor* model for galaxies with $M_* \sim 10^{11} M_{\odot}$ leads to a better agreement with observations than for the *fiducial* model. This points out that minor events occurring in massive galaxies should take place away from the galactic nucleus, hindering their possibility of resetting the TDE rates. While this might be true for massive systems, it is unlikely that for small galaxies catastrophic events such as major mergers or important disk instabilities are the unique processes able to significantly modify the stellar environment around nuclear MBHs and thus reset the relaxation process.

The underprediction of the volumetric TDE rates for small MBHs and galaxies shown in *OnlyMajor* model highlight that NSC structures (that dominate the overall TDE rates, see Sect. 3.1) should be dynamically influenced by their host galaxy interactions quite often. For instance, the accretion of non-major satellites and weak disk instabilities should result in a relatively frequent refilling of the loss cone of their hosted MBH. An important caveat to this argument is that catastrophic events are the type of interactions in which the basic assumptions of spherical symmetry and isotropy of stellar profiles (assumed in this work)

are most frequently violated and a rate enhancement may occur (see Sect. 5).

5. Limitations and Prospects

Here we discuss the main limitations which cannot be addressed with our methods. In addition, we discuss further details on the nature of TDE events which could potentially be captured in the framework of our model. We make some suggestions for improvements regarding both the use of PHASEFLOW and L-Galaxies, as well as motivate further research projects as an extension to this work.

5.1. Caveats regarding input TDE rates

As pointed out in Merritt (2013), the 1D Fokker Planck approach (see Sect. 2.2) may be inaccurate over the relaxation timescale. A more general treatment that accounts for the evolution of energy and angular momentum may be reliable on longer timescales, over which the angular momentum profile alters the overall evolution of the stellar profile (see e.g. Broggi et al. 2022). Moreover, there are effects that cannot be taken into account in PHASEFLOW, at least in its current form. Noticeable ones are: resonant relaxation of Keplerian orbits (Rauch & Tremaine 1996), large scattering (instead of diffusing into the loss-cone Weissbein & Sari 2017) or loss-cone shielding (Teboul et al. 2024); all of which have been shown to have an impact on TDE rates for specific systems. On top of this, relativistic effects may affect the outcome of the interactions and thus the prediction of the rate (e.g. Stone et al. 2019). Addressing all these caveats would require a different solution to the problem than the one provided with two-body energy relaxation as performed by PHASEFLOW.

In addition to the limitations due to the negligence of anisotropies, the current method is limited to working with spherical systems. Therefore, rates for axisymmetric profiles may deviate from the ones in this work (see e.g. Vasiliev & Merritt 2013). Kim et al. (2018) found evidence of elongated bulges being correlated with nuclear starbursts²⁰, which may be a possible way to allow an increase in rates for a specific type of bulges. In fact, the bursty behavior of high TDE rates in certain galaxy types has been explained through radial anisotropies (Stone et al. 2018), occurring through the formation of eccentric disks (Madigan et al. 2018; Rantala & Naab 2023), as opposed to overdensity at the nucleus (as assumed in this work). Nevertheless, it is worth noticing that observations have been favoring the latter (French et al. 2020a). All these are subjects that have mainly been explored by expensive N-body simulations with tailored initial conditions and go far beyond the general/average viewpoint we have drawn for the global TDE rates.

5.2. Caveats regarding the galaxy environment

Regarding the galaxy evolution model used in this work, one of the main aspects affecting the TDE demographics is the galaxy sizes predicted by L-Galaxies (initially introduced by Guo et al. 2011). Despite being traced self-consistently the expected sizes do not capture some particular galaxy classes discovered in the last decade (e.g. ultra-compact dwarfs). The inclusion of more refined environmental effects included in other *L-Galaxies* versions (e.g. Ayromlou et al. 2021, that adds ram-pressure strip-

²⁰ This relates to the open questions of the effects of stellar bars on central nuclear activity.

ping), may be necessary to capture the nature of these types of objects.

Regarding galaxy profiles, there are also some improvements in the modeling of stellar dynamics that can be included in our semi-analytical approach. Specifically, the Sérsic indices assigned to bulges by L-Galaxies are motivated by $z=0$ observations. However, this does not take into account the evolutionary history of galaxies. For instance, systems in a post-starburst and early quiescent phase (Setton et al. 2022), as well as “red nuggets” (e.g. Saracco et al. 2010; Barro et al. 2013; Ito et al. 2023; Baggen et al. 2023; Lohmann et al. 2023; Pandya et al. 2023), have been shown to display a larger Sérsic index than ordinary galaxies. Finally, the bulge velocity dispersion is not included self-consistently in L-Galaxies. This hinders the possibility of exploring the effect of this quantity on the TDE rates. For instance, observations of “ σ -drop” bulges (Comerón et al. 2008) suggest that some bulges will have a low enough velocity dispersion to significantly shorten relaxation timescales and thus change the expected TDEs (Cen 2020).

Regarding the reset mechanism (Sect. 2.3.2), internal processes such as phase-mixing, gravitational heating from perturbers (e.g. giant molecular clouds, Merritt 2013), and bar interactions with the nuclear region will certainly affect the event rates. These effects cannot be captured by our model since they are not quantified in L-Galaxies but rather would require modeling through expensive, dedicated hydrodynamical simulations including TDEs.

5.3. Rate enhancement

The highest per-galaxy rate predicted by our *fiducial* model corresponds to $\sim 10^{-4} \text{ yr}^{-1}$, compatible with the earliest results of Syer & Ulmer (1999). Despite that, a sample of galaxies like ULIRGs or E+A(k+a) post-starbursts seem to feature rates of 10^{-3} to 10^{-1} per year, values that are not reproduced in any individual galaxy of L-Galaxies, and rarely occur in the input grid of TDE rates (see Sect. 2.2.2). The large rate seen in post-starburst galaxies could be the result of a TDE enhancement driven by particular conditions. For instance, the recent theoretical work of French et al. (2017) supports the amplification of TDEs in the core of post-starburst galaxies, driven primarily by the compactness of these systems and not by the initial stellar mass function variations (Bortolas 2022). Another interpretation is that as soon as the AGN phase is over, the loss cone region around the MBH can be filled, thus boosting the expected TDE rates by up to two orders of magnitude compared to standard nuclei (Wang et al. 2024). Moreover, a significant fraction of MBHs are found in binaries at which the rates of the secondary MBH can be enhanced to be similar to those of the most massive one (see Li et al. 2017; Ryu et al. 2022; Mockler et al. 2023, and discussion further below). There are therefore three plausible explanations for the scarce number of cases with TDEs rates per MBH as high as $> 10^{-4} \text{ yr}^{-1}$ in our model²¹: i) the stellar profile of dwarf and intermediate-mass galaxies is not correctly captured at all times, ii) at least one enhancement mechanism due to additional physics is determining the global rates and should be included, or iii) the selected time resolution (limited by the maximum time-resolution of L-Galaxies, $dt_{\text{step}} \sim 10^7 \text{ yr}$) hinders the possibility of probing the initial prompt phase of violent relaxation for these objects. To examine the last explanation, a

cautious approach for the initial “bursty” phase when resetting the stellar environment around the MBH (see Sect. 2.2 & 2.3.2) may resolve this problem. This will be the subject of exploration in future work.

If the rates in the aforementioned over-represented classes of galaxies are indeed dominated by NSC rates, a more careful treatment of NSCs at different galaxy types could yield exceptionally high rates. Denser, cuspier, and more massive clusters are all conditions that have a non-negligible impact on the evolution of time-dependent TDE rates (Broggi et al. 2022). We have already noted that the introduced phenomenological model does not produce the most massive NSCs of mass $M_{\text{NSC}} = 10^8 - 10^9 M_{\odot}$ (see the mass function in Appendix A). In addition to that, the formation channel via accretion of clusters (assumed in this work) appears to operate in dwarf galaxies ($M_{\text{NSC}} < 10^8 - 10^9 M_{\odot}$, Johnston et al. 2020; Fahrion et al. 2021, 2022); yet central star formation may dominate cluster formation in larger galaxies (Aharon & Perets 2015; van Dokelaar et al. 2023). Consequently, the spheroidal profile used for this work could not be applied in such cases (see also Kacharov et al. 2018 and Pinna et al. 2021 for differences with host galaxy morphology). However, for the inclusion of cusplier profiles, mass segregation in angular momentum—which cannot be captured by PHASEFLOW—will prevent the model from computing correctly the TDE rates and a more sophisticated approach may be needed.

5.4. Other classes of star-MBH interactions:

In this work, we have focused our results on the rates of full TDEs and their contribution to MBH growth. However, there are many possible directions for future work exploring physically different types of interactions between stars and MBHs.

5.4.1. Partial Tidal Disruption Events

Partial tidal disruption events (partial TDEs) might be equally important for the growth of black holes as full TDEs. For example, Zhong et al. (2022) find that partial TDEs are super-Eddington 2.5 times more frequently than full TDEs, while the repetitive nature of these events can spoon-feed the MBH with increased efficiency MacLeod et al. (2012); Ryu et al. (2020b). Partial TDE rates are as high as those of full disruptions both theoretically (Krolik et al. 2020) and from recent observations (Somalwar et al. 2023b). Recently, (Bortolas et al. 2023) by tracing the fate of the remnants of such events and the inferred rates using PHASEFLOW showed that partial TDEs can be more frequent than full TDEs up to a few tens of times for nucleated galaxies. However, the radiative signatures of partial TDEs, and how they compare with those of full TDEs, need to be addressed before discussing further their statistics (e.g. a TDE can be falsely attributed as a rising AGN event, see e.g. Chen & Shen 2021). If indeed partial outnumber full TDEs, the volumetric TDE rates that we are comparing against may be overestimated. We continue this discussion quantitatively in Appendix B for the interested readers, where we introduce some relevant definitions.

In general, different orbit distributions will result in different frequencies of full TDEs, partial TDEs, and direct captures (Park & Hayasaki 2020; Cufari et al. 2022), but also different rates for certain subcategories of full TDEs, e.g. relativistic TDEs (Ryu et al. 2023a; Amaro Seoane 2023) and TDEs with eccentric debris disks (Zanazzi & Ogilvie 2020; Wevers et al. 2022). Tapping into the statistics of the orbits can serve as an additional time-dependent output in the grid-like exploration of the param-

²¹ These explanations rely on the assumption that high TDEs rates per MBH ($> 10^{-3} \text{ yr}^{-1}$) are not due to observationally unresolved NSCs (discussed later in this section).

eter space which then can be provided as L-Galaxies input, addressing the aforementioned issues. We plan to improve this model aspect in future works.

5.4.2. Rates from binary MBHs

The rich physics shaping the evolution of two (or more) MBHs toward coalescence following galaxy mergers, may significantly affect TDE rates. In the pairing phase, MBHs move within the potential of the bulge (not lying anymore in the dense center) and produce different rates of TDEs than central MBHs, with possible enhancement of rates during passages of stellar overdensities (Merritt 2013). After the formation of a binary (on parsec scales), the eccentric Kozai-Lidov mechanism can boost the rates of the secondary MBH to be similar to the most massive one (Chen et al. 2011; Mockler et al. 2023). Also at smaller separations (a multiple of the sum of the two MBHs tidal radii), the rates are theoretically expected to be boosted (Li et al. 2017; Ryu et al. 2022). An important enhancement would allow for an indirect inference of binaries through TDEs (Mockler et al. 2023), something to be investigated in follow-up work dedicated to rates from binary MBHs.

5.4.3. Electromagnetically-dark events

Extreme Mass Ratio Inspirals (EMRIs) and Direct Plunges (as defined in Broggi et al. 2022) of stellar remnants have their own evolution within an NSC. Given the relatively large mass accreted for each EMRI and plunge event, MBH growth via dark accretion of compact objects might even be more important than accretion through TDEs. However, while the distribution of stars in NSCs can be constrained by observations, there is no direct way to probe the distribution of non-luminous objects²²: this adds large theoretical uncertainties in calculating the cosmological rates. Also, regimes where general relativity effects are dominant over two-body relaxation should be taken into consideration.

Also of great interest, binary stars have a large tidal radius (Merritt 2013, 10-100 times that of a single star), while a binary system may be disrupted consecutively, either by one or both MBHs (Wu & Yuan 2018). For realistic EMRI and plunge rates, triple interactions between stellar remnant binaries and the MBH must be considered (Bonetti et al. 2019; Bonetti & Sesana 2020). Our method is currently not ideal for the inclusion of binary stars and remnants. We aim to investigate the aforementioned type of interactions, along with their contribution to the gravitational wave background to be probed by Laser Interferometry Space Antenna (LISA), in a future dedicated study.

6. Conclusions

In this work, we have included for the very first time tidal disruption events (TDEs) from massive black holes in a semi-analytic model of galaxy formation and evolution. To this end, we have used the *L-Galaxies* model (Henriques et al. 2015) in the version presented in Izquierdo-Villalba et al. (2020, 2022) and Spinoso et al. (2023), which includes many physical processes that drive the formation and evolution of massive black holes

(MBHs). For this work, we also included a phenomenological model for nuclear star clusters (NSCs) that uses the observed NSC-galaxy mass relations and reproduces the observed NSC occupation fraction. Time-dependent TDE rates for each galaxy are then obtained by solving the 1D Fokker-Planck equation with PHASEFLOW for a variety of stellar environments surrounding the MBHs. Finally, we employed simple post-processing assumptions for transforming theoretical to observable rates. The key findings of the model are summarized in the following:

- Our model predicts volumetric TDE rates that are in agreement with the observed ones. Rates from disruptions of stars belonging to the stellar disk or bulges alone can not explain the observed ones. Instead, we predict that the majority of TDEs should take place in NSCs, independently of galaxy or black hole mass. Specifically, to explain the rates within the local cosmological volume ($z < 0.5$), the model prefers an average NSC occupation as high as the one observed in the densest environments in the local universe (Coma cluster NSC occupation fraction by Hoyer et al. 2021). To derive the observed rates, we also find that a very high occupation fraction of black holes (100% capability of our physical model, see Spinoso et al. 2023, for details) and a steep black hole mass function ($\propto M_{\bullet}^{-1}$ at $M_{\bullet} \sim 10^5 - 10^{6.5} M_{\odot}$) are needed.
- The TDE rates per-MBH provided by any stellar reservoir (that is: either galaxy or NSC) do *not* follow a single power law as obtained in other works from scaling relations (e.g. $\dot{N}_{\text{per-MBH}} \propto M_{\bullet}^B$ with $-0.4 < B < 0$, see Wang & Merritt 2004; Stone & Metzger 2016; Pfister et al. 2020). Instead, our model produces a positive power-law dependence, with $B \approx 0.7$ for the TDE rates of the galaxy component that peak at $M_{\bullet} = 10^8 M_{\odot}$, before the event-horizon suppression completely takes over. For the NSC component (which dominates the TDE rates), we predict a power law index of $B = 0$ and $B = 1$ for young and old NSCs respectively, turning over at $M_{\bullet} \sim 10^7 M_{\odot}$. The model spin distribution with median spin $\bar{\chi}_{\bullet} = 0.6$ for MBHs of mass $M_{\bullet} = 10^7 - 10^{8.5} M_{\odot}$, naturally explains the event horizon suppression observed at optical TDE samples.
- A great fraction of TDEs ($\sim 100\%$ at the most massive hosts $M_{\bullet} > 10^{11} M_{\odot}$) take place around MBHs which are also experiencing some level of gas accretion. We thus predict TDEs to be detectable on top of low-luminosity AGN (bolometric luminosity $3 \times 10^{40} - 10^{42}$ erg/s), although AGN are generally excluded from TDE searches. Also, we predict TDE-like flares to have a volumetric rate of $1-3 \text{ Gpc}^{-3} \text{ yr}^{-1} \text{ dex}^{-1}$ for Seyfert galaxies with AGN luminosity $L_{\text{bol}} = 10^{42} - 10^{45}$ erg/s and galaxy mass $M_{\bullet} = 3 \times 10^{10} M_{\odot}$, with the rate slightly declining ($z = 0$) or staying constant ($z = 1$) for lower masses.

Our results highlight the importance of using a realistic cosmological framework to obtain a comprehensive view of TDE demographics. Furthermore, our results underline the importance of including time-dependent TDE rates (as demonstrated in Broggi et al. 2022), which allow us to account for the relaxation timescale in the statistics, unlike studies that use instantaneous TDE rates (e.g. Stone & Metzger 2016).

To conclude, the version of L-Galaxies presented here can overall reproduce the latest observed TDE rates, while respecting the constraints on the galaxy and black hole mass functions at $z = 0$. We highlight the need for a high NSC occupation fraction (close to $\sim 100\%$) in intermediate-mass galaxies hosting massive black holes, as well as the MBH spin model introduced in L-Galaxies by Izquierdo-Villalba et al. (2019) that naturally

²² This is the main reason these events were not included in our analysis because they do not fall into the same category as the optically detected TDEs. Yet, our model is already capable of investigating these phenomena, provided that it we track a population of stellar black holes within the NSC.

explains the observed drop of TDE rates towards the supermassive regime.

Finally, while we do not find a significant contribution of MBH mass growth via TDEs, the relation to galaxy hosts and the circumstances where TDE growth might be important for specific classes of MBHs and seeds will be investigated in a follow-up work (Polkas et al. in prep). We also plan to address the caveats and limitations of our model in future works to improve its ability to draw predictions for TDEs and the associated growth of MBHs, in particular in view of the upcoming flow of data from LSST.

Acknowledgements. This work used, as a foundation, the 2015 public version of the Munich model of galaxy formation and evolution: *L-Galaxies*. The source code and a full description of the model are available at <https://lgalaxiespublicrelease.github.io/>.

It also uses the publically available 1D-Fokker Planck solver PHASEFLOW available at <http://eugvas.net/software/phaseflow/>.

We thank Rosa Valiante for kindly allowing us to use her catalogues of GQd for the PopIII sub-grid physics.

M.P. and S.B. acknowledge support from the Spanish Ministerio de Ciencia e Innovación through project PID2021-124243NB-C21.

A.S. and D.I.V. acknowledge the financial support provided under the European Union's H2020 ERC Consolidator Grant "Binary Massive Black Hole Astrophysics" (B Massive, Grant Agreement: 818691).

N.H. is a fellow of the International Max Planck Research School for Astronomy and Cosmic Physics at the University of Heidelberg (IMPRS-HD). N.H. received financial support from the European Union's HORIZON-MSCA-2021-SE-01 Research and Innovation programme under the Marie Skłodowska-Curie grant agreement number 101086388 - Project acronym: LACEGAL.

D.S. acknowledges the support of the National Key R&D Program of China (grant no. 2018YFA0404503), the National Science Foundation of China (grant no. 12073014), the science research grants from the China Manned Space Project with No. CMS-CSST2021-A05, and Tsinghua University Initiative Scientific Research Program (No. 20223080023).

References

- Aharon, D. & Perets, H. B. 2015, *ApJ*, 799, 185
- Alexander, T. & Bar-Or, B. 2017, *Nature Astronomy*, 1, 0147
- Amaro Seoane, P. 2023, *arXiv e-prints*, arXiv:2307.13043
- Angulo, R. E. & White, S. D. M. 2010, *MNRAS*, 405, 143
- Antonini, F., Barausse, E., & Silk, J. 2015, *ApJ*, 812, 72
- Antonini, F., Capuzzo-Dolcetta, R., Mastrobuono-Battisti, A., & Merritt, D. 2012, *ApJ*, 750, 111
- Arca-Sedda, M. & Capuzzo-Dolcetta, R. 2014, *MNRAS*, 444, 3738
- Arcavi, I., Gal-Yam, A., Sullivan, M., et al. 2014, *ApJ*, 793, 38
- Ashok, A., Seth, A., Erwin, P., et al. 2023, *ApJ*, 958, 100
- Askar, A., Davies, M. B., & Church, R. P. 2022, *MNRAS*, 511, 2631
- Atallah, D., Trani, A. A., Kremer, K., et al. 2023, *MNRAS*, 523, 4227
- Auchettl, K., Guillochon, J., & Ramirez-Ruiz, E. 2017, *ApJ*, 838, 149
- Aversa, R., Lapi, A., de Zotti, G., Shankar, F., & Danese, L. 2015, *ApJ*, 810, 74
- Ayromlou, M., Kauffmann, G., Yates, R. M., Nelson, D., & White, S. D. M. 2021, *MNRAS*, 505, 492
- Bade, N., Komossa, S., & Dahlem, M. 1996, *A&A*, 309, L35
- Baggen, J. F. W., van Dokkum, P., Labbé, I., et al. 2023, *ApJ*, 955, L12
- Bahcall, J. N. & Wolf, R. A. 1976, *ApJ*, 209, 214
- Baldry, I. K., Glazebrook, K., & Driver, S. P. 2008, *MNRAS*, 388, 945
- Barro, G., Faber, S. M., Pérez-González, P. G., et al. 2013, *ApJ*, 765, 104
- Bassino, L. P., Muzzio, J. C., & Rabolli, M. 1994, *ApJ*, 431, 634
- Binney, J. & Tremaine, S. 2008, *Galactic Dynamics: Second Edition*
- Blanchard, P. K., Nicholl, M., Berger, E., et al. 2017, *ApJ*, 843, 106
- Bonetti, M. & Sesana, A. 2020, *Phys. Rev. D*, 102, 103023
- Bonetti, M., Sesana, A., Haardt, F., Barausse, E., & Colpi, M. 2019, *MNRAS*, 486, 4044
- Bonnerot, C., Pessah, M. E., & Lu, W. 2022, *ApJ*, 931, L6
- Bonoli, S., Marulli, F., Springel, V., et al. 2009, *Monthly Notices of the Royal Astronomical Society*, 396, 423
- Bortolas, E. 2022, *MNRAS*, 511, 2885
- Bortolas, E., Ryu, T., Broggi, L., & Sesana, A. 2023, *MNRAS*, 524, 3026
- Boylan-Kolchin, M., Springel, V., White, S. D. M., Jenkins, A., & Lemson, G. 2009, *MNRAS*, 398, 1150
- Bricman, K. & Gomboc, A. 2020, *ApJ*, 890, 73
- Brockamp, M., Baumgardt, H., & Kroupa, P. 2011, *MNRAS*, 418, 1308
- Broggi, L., Bortolas, E., Bonetti, M., Sesana, A., & Dotti, M. 2022, *MNRAS*, 514, 3270
- Bu, D.-F., Chen, L., Mou, G., Qiao, E., & Yang, X.-H. 2023, *MNRAS*, 521, 4180
- Bučar Bricman, K., van Velzen, S., Nicholl, M., & Gomboc, A. 2023, *ApJS*, 268, 13
- Bykov, S. D., Gilfanov, M. R., & Sunyaev, R. A. 2023, *MNRAS*[arXiv:2310.00303]
- Cannizzaro, G., Levan, A. J., van Velzen, S., & Brown, G. 2022, *MNRAS*, 516, 529
- Cao, X. 2010, *ApJ*, 725, 388
- Cao, X., You, B., & Wei, X. 2023, *MNRAS*, 526, 2331
- Capuzzo-Dolcetta, R. 1993, *ApJ*, 415, 616
- Carlsten, S. G., Greene, J. E., Beaton, R. L., & Greco, J. P. 2022, *ApJ*, 927, 44
- Carter, B. & Luminet, J. P. 1982, *Nature*, 296, 211
- Cen, R. 2020, *ApJ*, 888, L14
- Cenko, S. B., Bloom, J. S., Kulkarni, S. R., et al. 2012, *MNRAS*, 420, 2684
- Chan, C.-H., Piran, T., Krolik, J. H., & Saban, D. 2019, *ApJ*, 881, 113
- Chandrasekhar, S. 1942, *Principles of stellar dynamics*
- Charalampopoulos, P., Kotak, R., Wevers, T., et al. 2024, *arXiv e-prints*, arXiv:2401.11773
- Chen, J.-H. & Shen, R.-F. 2021, *ApJ*, 914, 69
- Chen, X., Sesana, A., Madau, P., & Liu, F. K. 2011, *ApJ*, 729, 13
- Chornock, R., Berger, E., Gezari, S., et al. 2014, *ApJ*, 780, 44
- Cohn, H. & Kulsrud, R. M. 1978, *The Astrophysical Journal*, 226, 1087
- Comerón, S., Knapen, J. H., & Beckman, J. E. 2008, *A&A*, 485, 695
- Coughlin, E. R. & Nixon, C. J. 2022, *ApJ*, 936, 70
- Croton, D. J., Springel, V., White, S. D. M., et al. 2006, *MNRAS*, 365, 11
- Cufari, M., Coughlin, E. R., & Nixon, C. J. 2022, *ApJ*, 924, 34
- Dai, L., McKinney, J. C., & Miller, M. C. 2015, *ApJ*, 812, L39
- Davis, B. L., Graham, A. W., & Cameron, E. 2019, *ApJ*, 873, 85
- den Brok, M., Peletier, R. F., Seth, A., et al. 2014, *MNRAS*, 445, 2385
- Dgany, Y., Arcavi, I., Makrygianni, L., Pellegrino, C., & Howell, D. A. 2023, *arXiv e-prints*, arXiv:2307.00594
- Dodd, S. A., Law-Smith, J. A. P., Auchettl, K., Ramirez-Ruiz, E., & Foley, R. J. 2021, *ApJ*, 907, L21
- Donley, J. L., Brandt, W. N., Eracleous, M., & Boller, T. 2002, *AJ*, 124, 1308

- Efstathiou, G., Lake, G., & Negroponte, J. 1982, *MNRAS*, 199, 1069
- Eigenthaler, P., Puzia, T. H., Taylor, M. A., et al. 2018, *ApJ*, 855, 142
- Esquej, P., Saxton, R. D., Komossa, S., et al. 2008, *A&A*, 489, 543
- Fahrion, K., Bulichi, T.-E., Hilker, M., et al. 2022, *A&A*, 667, A101
- Fahrion, K., Lyubenova, M., van de Ven, G., et al. 2021, *A&A*, 650, A137
- Frank, J. & Rees, M. J. 1976, *MNRAS*, 176, 633
- Frederick, S., Gezari, S., Graham, M. J., et al. 2021, *ApJ*, 920, 56
- French, K. D., Arcavi, I., & Zabludoff, A. 2016, *ApJ*, 818, L21
- French, K. D., Arcavi, I., & Zabludoff, A. 2017, *ApJ*, 835, 176
- French, K. D., Arcavi, I., Zabludoff, A. I., et al. 2020a, *ApJ*, 891, 93
- French, K. D., Wevers, T., Law-Smith, J., Graur, O., & Zabludoff, A. I. 2020b, *Space Sci. Rev.*, 216, 32
- Gadotti, D. A. 2009, *MNRAS*, 393, 1531
- Gallo, E. & Sesana, A. 2019, *ApJ*, 883, L18
- Gebhardt, K., Lauer, T. R., Kormendy, J., et al. 2001, *AJ*, 122, 2469
- Generozov, A. & Perets, H. B. 2023, *MNRAS*, 522, 1763
- Georgiev, I. Y., Böker, T., Leigh, N., Lützgendorf, N., & Neumayer, N. 2016, *MNRAS*, 457, 2122
- Gezari, S., Basa, S., Martin, D. C., et al. 2008, *ApJ*, 676, 944
- Gezari, S., Martin, D. C., Milliard, B., et al. 2006, *ApJ*, 653, L25
- Goldtooth, A., Zabludoff, A. I., Wen, S., et al. 2023, *PASP*, 135, 034101
- Graham, A. W. & Spitler, L. R. 2009, *MNRAS*, 397, 2148
- Graur, O., French, K. D., Zahid, H. J., et al. 2018, *ApJ*, 853, 39
- Greene, J. E. 2012, *Nature Communications*, 3, 1304
- Greene, J. E., Strader, J., & Ho, L. C. 2020, *ARA&A*, 58, 257
- Guillochon, J. & Ramirez-Ruiz, E. 2013, *ApJ*, 767, 25
- Guo, Q., White, S., Boylan-Kolchin, M., et al. 2011, *MNRAS*, 413, 101
- Guolo, M., Gezari, S., Yao, Y., et al. 2023, arXiv e-prints, arXiv:2308.13019
- Haiman, Z., Rees, M. J., & Loeb, A. 1997, *ApJ*, 476, 458
- Hambleton, K. M., Bianco, F. B., Street, R., et al. 2023, *PASP*, 135, 105002
- Hammerstein, E., Gezari, S., van Velzen, S., et al. 2021, *ApJ*, 908, L20
- Hammerstein, E., van Velzen, S., Gezari, S., et al. 2023, *ApJ*, 942, 9
- Hartmann, M., Debattista, V. P., Seth, A., Cappellari, M., & Quinn, T. R. 2011, *MNRAS*, 418, 2697
- Henriques, B. M. B., White, S. D. M., Thomas, P. A., et al. 2015, *MNRAS*, 451, 2663
- Henriques, B. M. B., Yates, R. M., Fu, J., et al. 2020, *MNRAS*, 491, 5795
- Hills, J. G. 1975, *Nature*, 254, 295
- Hinkle, J. T., Holoien, T. W. S., Auchettl, K., et al. 2021, *MNRAS*, 500, 1673
- Hinkle, J. T., Holoien, T. W. S., Shappee, B. J., et al. 2022, *ApJ*, 930, 12
- Homan, D., Krumpke, M., Markowitz, A., et al. 2023, *A&A*, 672, A167
- Hoyer, N., Neumayer, N., Georgiev, I. Y., Seth, A. C., & Greene, J. E. 2021, *MNRAS*, 507, 3246
- Hoyer, N., Neumayer, N., Seth, A. C., Georgiev, I. Y., & Greene, J. E. 2023, *MNRAS*, 520, 4664
- Huang, H.-T. & Lu, W. 2024, *MNRAS*, 527, 1865
- Huang, S., Jiang, N., Lin, Z., Zhu, J., & Wang, T. 2023, *MNRAS*, 525, 4057
- Ito, K., Valentino, F., Brammer, G., et al. 2023, arXiv e-prints, arXiv:2307.06994
- Izquierdo-Villalba, D., Bonoli, S., Dotti, M., et al. 2020, *MNRAS*, 495, 4681
- Izquierdo-Villalba, D., Bonoli, S., Spinoso, D., et al. 2019, *MNRAS*, 488, 609
- Izquierdo-Villalba, D., Sesana, A., Bonoli, S., & Colpi, M. 2022, *MNRAS*, 509, 3488
- Jankovič, T., Bonnerot, C., & Gomboc, A. 2023, arXiv e-prints, arXiv:2303.16230
- Johnston, E. J., Puzia, T. H., D’Ago, G., et al. 2020, *MNRAS*, 495, 2247
- Kacharov, N., Neumayer, N., Seth, A. C., et al. 2018, *MNRAS*, 480, 1973
- Karas, V. & Šubr, L. 2007, *A&A*, 470, 11
- Kaviraj, S., Kirkby, L. A., Silk, J., & Sarzi, M. 2007, *MNRAS*, 382, 960
- Kawamuro, T., Ueda, Y., Shidatsu, M., et al. 2016, *PASJ*, 68, 58
- Kesden, M. 2012, *Phys. Rev. D*, 85, 024037
- Khan, F. M. & Holley-Bockelmann, K. 2021, *MNRAS*, 508, 1174
- Kim, E., Kim, S. S., Choi, Y.-Y., et al. 2018, *MNRAS*, 479, 562
- Kimbrell, S. J., Reines, A. E., Schutte, Z., Greene, J. E., & Geha, M. 2021, *ApJ*, 911, 134
- Kiroğlu, F., Lombardi, J. C., Kremer, K., et al. 2023, *ApJ*, 948, 89
- Kochanek, C. S. 2016, *MNRAS*, 461, 371
- Komossa, S. & Bade, N. 1999, *A&A*, 343, 775
- Kool, E. C., Reynolds, T. M., Mattila, S., et al. 2020, *MNRAS*, 498, 2167
- Kormendy, J. & Ho, L. C. 2013, *ARA&A*, 51, 511
- Kritos, K., Berti, E., & Silk, J. 2023, *Phys. Rev. D*, 108, 083012
- Krolik, J., Piran, T., & Ryu, T. 2020, *ApJ*, 904, 68
- Krolik, J., Piran, T., Svirski, G., & Cheng, R. M. 2016, *ApJ*, 827, 127
- Kroupa, P. 2001, *MNRAS*, 322, 231
- Law-Smith, J., Ramirez-Ruiz, E., Ellison, S. L., & Foley, R. J. 2017, *ApJ*, 850, 22
- Leaman, R. & van de Ven, G. 2022, *MNRAS*, 516, 4691
- Lee, S., Kim, J.-h., & Oh, B. K. 2023, *ApJ*, 943, 77
- Li, J., Wang, Z.-X., Zheng, D., et al. 2023, *Research in Astronomy and Astrophysics*, 23, 025012
- Li, S., Liu, F. K., Berczik, P., & Spurzem, R. 2017, *ApJ*, 834, 195
- Lin, Z., Jiang, N., Kong, X., et al. 2022, *ApJ*, 939, L33
- Liu, C., Mockler, B., Ramirez-Ruiz, E., et al. 2023, *ApJ*, 944, 184
- Liu, Z., Li, D., Liu, H.-Y., et al. 2020, *ApJ*, 894, 93
- Lohmann, F. S., Schnorr-Müller, A., Trevisan, M., Ricci, T. V., & Clerici, K. S. 2023, *MNRAS*, 524, 5266
- MacLeod, M., Guillochon, J., & Ramirez-Ruiz, E. 2012, *ApJ*, 757, 134
- Madigan, A.-M., Halle, A., Moody, M., et al. 2018, *ApJ*, 853, 141
- Magorrian, J. & Tremaine, S. 1999, *MNRAS*, 309, 447
- Mainetti, D., Lupi, A., Campana, S., et al. 2017, *A&A*, 600, A124
- Makrygianni, L., Trakhtenbrot, B., Arcavi, I., et al. 2023, *ApJ*, 953, 32
- Malyali, A., Liu, Z., Rau, A., et al. 2023, *MNRAS*, 520, 3549
- Masterson, M., De, K., Panagiotou, C., et al. 2024, arXiv e-prints, arXiv:2401.01403

- Mattila, S., Pérez-Torres, M., Efstathiou, A., et al. 2018, *Science*, 361, 482
- Mayes, R. J., Drinkwater, M. J., Pfeffer, J., et al. 2021, *MNRAS*, 506, 2459
- McKernan, B., Ford, K. E. S., Cantiello, M., et al. 2022, *MNRAS*, 514, 4102
- Merloni, A. & Heinz, S. 2008, *MNRAS*, 388, 1011
- Merritt, D. 2009, *ApJ*, 694, 959
- Merritt, D. 2013, *Classical and Quantum Gravity*, 30, 244005
- Merritt, D., Ferrarese, L., & Joseph, C. L. 2001, *Science*, 293, 1116
- Mezcua, M., Civano, F., Marchesi, S., et al. 2018, *MNRAS*, 478, 2576
- Mezcua, M. & Domínguez Sánchez, H. 2020, *ApJ*, 898, L30
- Miller, M. C. & Davies, M. B. 2012, *ApJ*, 755, 81
- Milosavljević, M., Merritt, D., & Ho, L. C. 2006, *ApJ*, 652, 120
- Mockler, B., Melchor, D., Naoz, S., & Ramirez-Ruiz, E. 2023, *ApJ*, 959, 18
- Mockler, B. & Ramirez-Ruiz, E. 2021, *ApJ*, 906, 101
- Mockler, B., Twum, A. A., Auchettl, K., et al. 2022, *ApJ*, 924, 70
- Moustakas, J., Coil, A. L., Aird, J., et al. 2013, *ApJ*, 767, 50
- Muñoz, R. P., Eigenthaler, P., Puzia, T. H., et al. 2015, *ApJ*, 813, L15
- Mummery, A. 2024, *MNRAS*, 527, 6233
- Mummery, A. & Balbus, S. A. 2020, *MNRAS*, 497, L13
- Mummery, A., van Velzen, S., Nathan, E., et al. 2024, *MNRAS*, 527, 2452
- Mutlu-Pakdil, B., Seigar, M. S., & Davis, B. L. 2016, *ApJ*, 830, 117
- Naiman, J. P., Ramirez-Ruiz, E., Debuhr, J., & Ma, C. P. 2015, *ApJ*, 803, 81
- Nasim, S. S., Fabj, G., Caban, F., et al. 2023, *MNRAS*, 522, 5393
- Neumayer, N., Seth, A., & Böker, T. 2020, *A&A Rev.*, 28, 4
- Neumayer, N. & Walcher, C. J. 2012, *Advances in Astronomy*, 2012, 709038
- Nguyen, D. D., Bureau, M., Thater, S., et al. 2022, *MNRAS*, 509, 2920
- Nguyen, D. D., Seth, A. C., Neumayer, N., et al. 2018, *ApJ*, 858, 118
- Oates, S. R., Kuin, N. P. M., Nicholl, M., et al. 2023, arXiv e-prints, arXiv:2307.01044
- Panagiotou, C., De, K., Masterson, M., et al. 2023, *ApJ*, 948, L5
- Pandya, V., Zhang, H., Huertas-Company, M., et al. 2023, arXiv e-prints, arXiv:2310.15232
- Park, G. & Hayasaki, K. 2020, *ApJ*, 900, 3
- Payne, A. V., Shappee, B. J., Hinkle, J. T., et al. 2021, *ApJ*, 910, 125
- Pechetti, R., Seth, A., Neumayer, N., et al. 2020, *ApJ*, 900, 32
- Pérez-González, P. G., Trujillo, I., Barro, G., et al. 2008, *ApJ*, 687, 50
- Pfeffer, J., Griffen, B. F., Baumgardt, H., & Hilker, M. 2014, *MNRAS*, 444, 3670
- Pfister, H., Dai, J. L., Volonteri, M., et al. 2021, *MNRAS*, 500, 3944
- Pfister, H., Toscani, M., Wong, T. H. T., et al. 2022, *MNRAS*, 510, 2025
- Pfister, H., Volonteri, M., Dai, J. L., & Colpi, M. 2020, *MNRAS*, 497, 2276
- Phinney, E. S. 1989, in *The Center of the Galaxy*, ed. M. Morris, Vol. 136, 543
- Pinna, F., Neumayer, N., Seth, A., et al. 2021, *ApJ*, 921, 8
- Planck Collaboration, Aghanim, N., Akrami, Y., et al. 2020, *A&A*, 641, A6
- Prasad, C., Wang, Y., Perna, R., Ford, K. E. S., & McKernan, B. 2023, arXiv e-prints, arXiv:2310.00020
- Rantala, A. & Naab, T. 2023, arXiv e-prints, arXiv:2308.12344
- Rauch, K. P. & Tremaine, S. 1996, *New A*, 1, 149
- Rees, M. J. 1988, *Nature*, 333, 523
- Reines, A. E. & Volonteri, M. 2015, *ApJ*, 813, 82
- Reynolds, C. S. 2021, *ARA&A*, 59, 117
- Reynolds, T. M., Mattila, S., Efstathiou, A., et al. 2022, *A&A*, 664, A158
- Ricci, C. & Trakhtenbrot, B. 2023, *Nature Astronomy*, 7, 1282
- Rizzuto, F. P., Naab, T., Rantala, A., et al. 2023, *MNRAS*, 521, 2930
- Roediger, J. C. & Courteau, S. 2015, *MNRAS*, 452, 3209
- Ryu, T., Krolik, J., & Piran, T. 2023a, *ApJ*, 946, L33
- Ryu, T., Krolik, J., Piran, T., & Noble, S. C. 2020a, *ApJ*, 904, 98
- Ryu, T., Krolik, J., Piran, T., & Noble, S. C. 2020b, *ApJ*, 904, 100
- Ryu, T., McKernan, B., Ford, K. E. S., et al. 2023b, *MNRAS*[arXiv:2310.00610]
- Ryu, T., Trani, A. A., & Leigh, N. W. C. 2022, *MNRAS*, 515, 2430
- Saha, P. 1992, *MNRAS*, 254, 132
- Sánchez-Janssen, R., Côté, P., Ferrarese, L., et al. 2019, *ApJ*, 878, 18
- Saracco, P., Longhetti, M., & Gargiulo, A. 2010, *MNRAS*, 408, L21
- Sazonov, S., Gilfanov, M., Medvedev, P., et al. 2021, *MNRAS*, 508, 3820
- Seth, A., Agüeros, M., Lee, D., & Basu-Zych, A. 2008, *ApJ*, 678, 116
- Setton, D. J., Verrico, M., Bezanson, R., et al. 2022, *ApJ*, 931, 51
- Shankar, F., Bernardi, M., Richardson, K., et al. 2019, *MNRAS*, 485, 1278
- Shankar, F., Bernardi, M., Sheth, R. K., et al. 2016, *MNRAS*, 460, 3119
- Shankar, F., Weinberg, D. H., & Miralda-Escudé, J. 2009, *ApJ*, 690, 20
- Shankar, F., Weinberg, D. H., & Miralda-Escudé, J. 2013, *MNRAS*, 428, 421
- Shen, S., Mo, H. J., White, S. D. M., et al. 2003, *MNRAS*, 343, 978
- Singh, T. & Kesden, M. 2023, arXiv e-prints, arXiv:2306.08054
- Siudek, M., Mezcua, M., & Krywult, J. 2023, *MNRAS*, 518, 724
- Somalwar, J. J., Ravi, V., & Lu, W. 2023a, arXiv e-prints, arXiv:2310.03795
- Somalwar, J. J., Ravi, V., Yao, Y., et al. 2023b, arXiv e-prints, arXiv:2310.03782
- Spergel, D. N., Verde, L., Peiris, H. V., et al. 2003, *ApJS*, 148, 175
- Spinoso, D., Bonoli, S., Valiante, R., Schneider, R., & Izquierdo-Villalba, D. 2023, *MNRAS*, 518, 4672
- Springel, V., White, S. D. M., Jenkins, A., et al. 2005, *Nature*, 435, 629
- Steinberg, E. & Stone, N. C. 2022, arXiv e-prints, arXiv:2206.10641
- Stone, N., Sari, R., & Loeb, A. 2013, *MNRAS*, 435, 1809
- Stone, N. C., Generozov, A., Vasiliev, E., & Metzger, B. D. 2018, *MNRAS*, 480, 5060
- Stone, N. C., Kesden, M., Cheng, R. M., & van Velzen, S. 2019, *General Relativity and Gravitation*, 51, 30
- Stone, N. C., Küpper, A. H. W., & Ostriker, J. P. 2017, *MNRAS*, 467, 4180
- Stone, N. C. & Metzger, B. D. 2016, *MNRAS*, 455, 859

- Stone, N. C., Vasiliev, E., Kesden, M., et al. 2020, *Space Sci. Rev.*, 216, 35
- Sutherland, R. S. & Dopita, M. A. 1993, *ApJS*, 88, 253
- Syer, D. & Ulmer, A. 1999, *MNRAS*, 306, 35
- Tadhunter, C., Spence, R., Rose, M., Mullaney, J., & Crowther, P. 2017, *Nature Astronomy*, 1, 0061
- Teboul, O., Stone, N. C., & Ostriker, J. P. 2024, *MNRAS*, 527, 3094
- Thater, S., Lyubenova, M., Fahrion, K., et al. 2023, *A&A*, 675, A18
- Trani, A. A., Mapelli, M., & Ballone, A. 2018, *ApJ*, 864, 17
- Tremmel, M., Ricarte, A., Natarajan, P., et al. 2023, *arXiv e-prints*, arXiv:2306.12813
- Trump, J. R., Sun, M., Zeimann, G. R., et al. 2015, *ApJ*, 811, 26
- Urquhart, R., McDermott, L. I., Strader, J., et al. 2022, *ApJ*, 940, 111
- Valiante, R., Schneider, R., Volonteri, M., & Omukai, K. 2016, *MNRAS*, 457, 3356
- Valluri, M., Ferrarese, L., Merritt, D., & Joseph, C. L. 2005, *ApJ*, 628, 137
- van Dokelaar, F., Mayer, L., Capelo, P. R., et al. 2023, *arXiv e-prints*, arXiv:2303.12828
- van Velzen, S. 2018, *ApJ*, 852, 72
- van Velzen, S. & Farrar, G. R. 2014, *ApJ*, 792, 53
- van Velzen, S., Farrar, G. R., Gezari, S., et al. 2011, *ApJ*, 741, 73
- Vasiliev, E. 2017, *ApJ*, 848, 10
- Vasiliev, E. 2019, *MNRAS*, 482, 1525
- Vasiliev, E. & Merritt, D. 2013, *ApJ*, 774, 87
- Vika, M., Driver, S. P., Graham, A. W., & Liske, J. 2009, *MNRAS*, 400, 1451
- Wang, J. & Merritt, D. 2004, *ApJ*, 600, 149
- Wang, M., Ma, Y., Wu, Q., & Jiang, N. 2024, *ApJ*, 960, 69
- Wang, Y., Jiang, N., Wang, T., et al. 2022, *ApJ*, 930, L4
- Weissbein, A. & Sari, R. 2017, *MNRAS*, 468, 1760
- Wevers, T., Nicholl, M., Guolo, M., et al. 2022, *A&A*, 666, A6
- Wevers, T., Stone, N. C., van Velzen, S., et al. 2019, *MNRAS*, 487, 4136
- White, S. D. M. & Frenk, C. S. 1991, *ApJ*, 379, 52
- White, S. D. M. & Rees, M. J. 1978, *MNRAS*, 183, 341
- Wild, V., Almaini, O., Dunlop, J., et al. 2016, *MNRAS*, 463, 832
- Wild, V., Taj Aldeen, L., Carnall, A., et al. 2020, *MNRAS*, 494, 529
- Wong, T. H. T., Pfister, H., & Dai, L. 2022, *ApJ*, 927, L19
- Wu, X.-J. & Yuan, Y.-F. 2018, *MNRAS*, 479, 1569
- XueGuang, Z. 2022, *arXiv e-prints*, arXiv:2209.09037
- Yao, Y., Ravi, V., Gezari, S., et al. 2023, *ApJ*, 955, L6
- Zajaček, M., Czerny, B., Jaiswal, V. K., et al. 2023, *arXiv e-prints*, arXiv:2306.15082
- Zanatta, E., Sánchez-Janssen, R., Chies-Santos, A. L., de Souza, R. S., & Blakeslee, J. P. 2021, *MNRAS*, 508, 986
- Zanazzi, J. J. & Ogilvie, G. I. 2020, *MNRAS*, 499, 5562
- Zhao, H. 1996, *MNRAS*, 278, 488
- Zhong, S., Li, S., Berczik, P., & Spurzem, R. 2022, *ApJ*, 933, 96
- Zou, F., Brandt, W. N., Ni, Q., et al. 2023, *ApJ*, 950, 136

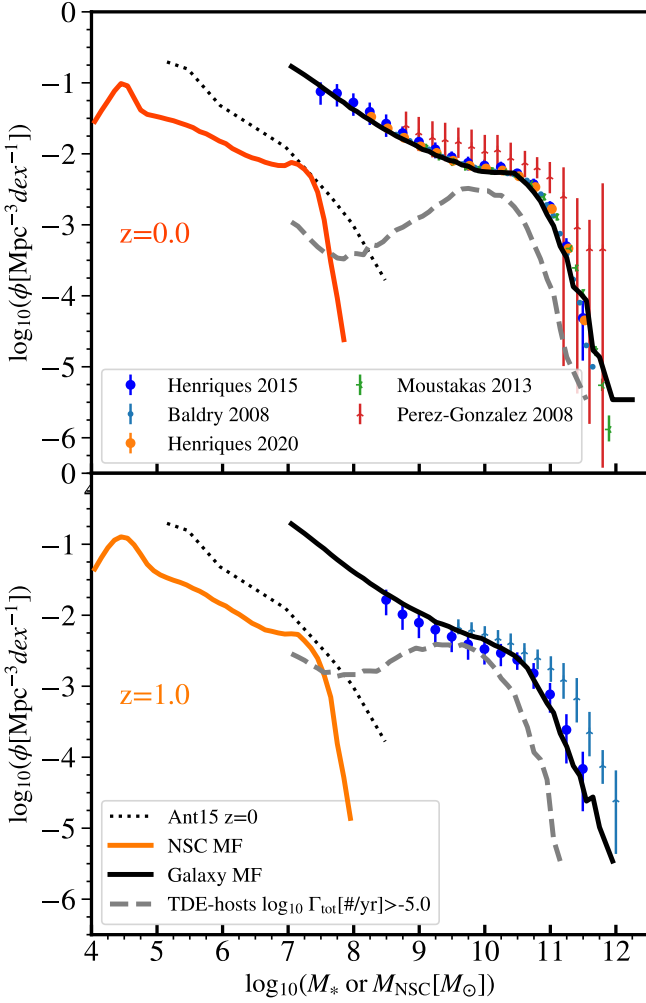


Fig. A.1. Stellar Mass Functions of all galaxies (solid black) and TDE-host galaxies with the highest TDE rates ($\Gamma_{\text{tot}} > 10^{-5}$, grey dashed) for the *fiducial* model at $z=0$ and $z=1$. The first is compared with compiled mass constraints from Henriques et al. (2015) and Henriques et al. (2020), Baldry et al. (2008), Pérez-González et al. (2008), and Moustakas et al. (2013) (inset legend). With a thin colored line at lower masses, the NSC Mass Function of the *fiducial* model is plotted at the same redshifts. For comparison, we display the model NSC mass function from Antonini et al. (2015) at $z=0$ (Ant15 $z=0$).

Appendix A: TDE hosts mass functions

Our model can explain the constraints of Yao et al. (2023) on the galaxy stellar mass distribution of the volumetric rates. We discuss briefly the reasons for the relatively good agreement and the issues to be addressed regarding the TDE host mass range in future works.

As observed in Fig. A.1 (grey dashed), we reproduce the flat galaxy stellar mass function expected for TDE host galaxies as inferred from observations (Law-Smith et al. 2017). Galaxy stellar mass functions are all in good agreement with one another and with observations at $z=0, 1$, as expected by the success of the *L-Galaxies* models.

In the same plot, we present the NSC mass function at $z=0$ (dotted-dashed) which is lower compared to the theoretical predictions of Antonini et al. (2015) by an order of magnitude at lower masses, obviously having a different slope. The number density provided by this function should be a theoretical lower limit to reproduce the TDE rates, yet NSCs without MBHs

should also be considered. The model predicts that NSCs do not evolve significantly with redshift from $z=1$, as they are tightly related to the nuclear MBHs (that also do not evolve).

At $z=0$ the peak at hosts with high rates within $M_* = 10^{9.5} - 10^{10.5} M_\odot$ is directly related to hosting massive NSC $M_{\text{NSC}} = 10^7 - 10^8 M_\odot$ and recently seeded (high per-galaxy rates, left panel in Fig. A.1 for NSC distribution) while the evolving tail ($M_* < 10^9 M_\odot$ from $z=1$ to $z=0$ is from the contribution of intermediate-mass MBHs and smaller NSC (right NSC distribution in Fig. A.1), and systems with TDE rates decaying with time. The model predicts mild redshift evolution, a falsifiable argument with the observations of TDEs up to $z=1$ from the forthcoming LSST samples.

Appendix B: Useful definitions for Tidal Disruption Event rate interpretation

An interaction between a massive black hole and a star reaches its proximity zone of less than one tidal radius r_t (Eq. 3 in the main text), at fixed masses M_\bullet and m_* respectively, will result in a variety of outcomes, with different energetics and observable signatures depending on many parameters. How close to the horizon the star is destined to make a passage is of particular importance (Carter & Luminet 1982; Stone et al. 2013; Dai et al. 2015). It is useful to quantify this with the penetration parameter that is defined as

$$\beta = r_t / r_p,$$

where r_p the pericenter of the orbit and

$$r_t = 6.9 \times 10^{12} \text{ cm } \eta_{\text{TD}}^{2/3} (M_\bullet / 10^6 M_\odot)^{1/3} m_*^{-1/3} r_*$$

the tidal radius depends on the mass/radius of the star disrupted m_* and r_* (units of $1 M_\odot$ and $1 R_\odot$). The coefficient η_{TD} depends on the polytropic index of the star and is of the order unity (Merritt 2013). Penetration factor values range from $\beta_{\text{min}} = 0.5 - 0.6$ as derived from hydrodynamical simulations (Guillochon & Ramirez-Ruiz 2013) and at which point stars are merely disrupted, to β_{max} at which point stars enter whole into the MBH's horizon. Analytical calculation on horizon suppression for a Schwarzschild MBH yields (Kesden 2012; Mummery 2024)

$$\beta_{\text{max}} = 11.8 M_{\bullet,6}^{-2/3} m_*^{-1/3} r_*. \quad (\text{B.1})$$

Also, below a value β_c the star is not fully disrupted. Therefore, full TDEs at the interval $\beta_c < \beta < \beta_{\text{max}}$ while direct captures occur for $\beta > \beta_{\text{max}}(M_\bullet)$. The rest of the events are found in the interval $\beta_{\text{min}} < \beta_c$ and are considered partial TDEs. The latter are identified by the re-flaring of their source and less frequently from their differentiation in the fading power law ($-9/4$ instead of $-5/3$). Ryu et al. (2020a) has shown that the physical tidal radius at which the star is fully disrupted has both stellar and MBH mass dependence. For disrupted stars of mass 0.3 and $1 M_\odot$, we adopt

$$\beta_c = \beta_{c,0} \frac{1}{1 + C_0 (M_\bullet / 10^6 M_\odot)^{2/3}}. \quad (\text{B.2})$$

where $\beta_{c,0} = 2.0, C_0 = 0.166$ & $\beta_{c,0} = 2.65, C_0 = 0.204$ respectively. We set the simple form $\beta_{c,0}(m_*) = 1.6(m_* + 0.45)$ and fix $C_0 = 0.2$ for our simple calculations here (although there is not a linear transition between stars with different polytropic indices). For reference, Guillochon & Ramirez-Ruiz (2013) and Mainetti et al. (2017) values from simulations for convective & radiation-dominated stars around a $M_\bullet = 10^6 M_\odot$ MBH translate

into $\beta_{c,0} = 1.08$ & 2.2 when fixing $C_0 = 0.2$ respectively. Note that there is a continuous transition from TDEs to direct captures as $\beta_c(m_*) \rightarrow \beta_{\max}(M_\bullet, m_*, \chi_\bullet, t)$, with the Hills mass being rather a range of values for the distribution of star masses. *This transition is computed solely in the analysis here*; in the main text TDEs are considered as $\beta > \beta_c = 1$ (all stars within the tidal radius are disrupted) with $\beta_{\max} \rightarrow \infty$ for $M_\bullet < 10^8 M_\odot$ (direct captures are not considered separately) and $\beta_{\max} < \beta_c$ for higher MBH masses (all events are considered direct captures).

The number of orbits per penetration factor bin $dN(\beta)/d\beta$ takes the analytical form of a power-law for the full loss-cone regime (the system just started to relax). By assuming uniformity of the orbits over r_p gives a power-law dependence of $\propto \beta^{-2}$ (Stone et al. 2020). When the relativistic gravity is taken into account, this power law drops to $\beta^{-10/3}$ (Coughlin & Nixon 2022) for maximally-spinning MBHs (Kerr metric). Also, we consider the scenario where orbits are distributed uniformly over surface $2\pi r_p dr_p$ and the probability function scales as $\propto \beta^{-3}$ (Bricman & Gomboc 2020). At the empty loss-cone regime (the system has relaxed) there is a weak (logarithmic) dependence of rates on β , so essentially we can assume $\propto \beta^0$ for this case. For simplicity, we assume that the distribution of orbits destined to do partial TDEs follows from one of the full TDEs as inferred for the disruption of normal stars from Zhong et al. (2022).

We can now write the fraction of full TDEs as the integral of a power-law probability $\beta^{-S_\beta-1}$ in the value intervals mentioned above:

$$f_{\text{FTDE}}(m_*, M_\bullet) = \frac{\beta_c(m_*, M_\bullet)^{-S_\beta} - \beta_{\max}(m_*, M_\bullet)^{-S_\beta}}{\beta_{\min}^{-S_\beta} - \beta_{\max}(m_*, M_\bullet)^{-S_\beta}} \quad (\text{B.3})$$

where the generic power-law S_β is in the range $S_\beta \in [1, 2]$ for our calculations, for a non-empty loss cone (for all types of events). For the empty loss-cone regime, $S_\beta = -1$ and events at all β should be equally rare.

Now, we can estimate a general correction for our calculated rates of full disruption stars to the rate of all disruptions by using Eq.B.3, for the regime where $\beta_{\min} \gg \beta_c \gg \beta_{\max}$ get that full/total TDE rate converges as $f_{\text{FTDE}} \rightarrow (\beta_{\min}/\beta_c)^{S_\beta}$. For $\beta_{\min} = 0.6$ and $M_\bullet \lesssim 10^6 M_\odot$ yields almost invariably²³ a correction factor of

$$1/f_{\text{FTDE}} \in [2, 4]$$

for $S_\beta \in [1, 2]$. This correction could be applied only to “young” systems relaxing only for the last < 100 Myr that have not emptied their loss-cone. However, the physics of circularization could be different for TDEs varying in β , especially for the unknown regime of lower MBH masses (Kiroğlu et al. 2023, $M_\bullet = 10^2 - 10^4 M_\odot$) and the rates may be modified accordingly (Wong et al. 2022). These simulations²⁴ show a critical value greater than the one adopted from studies at $M_\bullet = 10^6 M_\odot$, namely $\beta_c \sim 10/3 > 47/19.1$, making the fraction of full disruptions even smaller and this correction greater. Furthermore, this correction factor can be a few tens (> 1 dex), as demonstrated by the self-consistent work on partial disruption events by Bor-tolas et al. (2023). By visual inspection, in the optical sample of Yao et al. (2023) there are more than a few light curves that

show a re-flaring activity, instead of a monotonic drop of luminosity. Caution should be drawn when comparing model event rates with samples of TDEs.

²³ This refers to both convection-dominated and radiation-dominated stars since the fraction of full TDE rates is already over-estimated by a factor of $(\beta_c)^{S_\beta}$ when assuming the TDE rates of $0.38 M_\odot$ stars hold for more massive stars PHASEFLOW. Also, the weak dependence of β_c on MBH mass in the regime is neglected.

²⁴ Both studies use general relativistic hydrodynamics and initial conditions from the stellar code MESA.